

**Development and Characterization of Additive Manufacturing of
Superalloy Hastelloy X Using a Cost Effective TIG Technique**

by

Malcolm Dinovitzer

A thesis submitted to the Faculty of Graduate and Postdoctoral
Affairs in partial fulfillment of the requirements for the degree of

Master of Applied Science

in

Aerospace Engineering

Department of Mechanical and Aerospace Engineering
Carleton University
Ottawa, Ontario, Canada

© 2020, Malcolm Dinovitzer

The undersigned recommend to
the Faculty of Graduate Studies and Research
acceptance of the Thesis

**Development and Characterization of Additive Manufacturing of
Superalloy Hastelloy X Using a Cost Effective TIG Technique**

Submitted by Malcolm Dinovitzer
in partial fulfilment of the requirements of the degree of
Master of Applied Science

Dr. X. Huang, Thesis Co-Supervisor

Dr. J. Laliberté, Thesis Co-Supervisor

Dr. R. Miller, Department Chair

Carleton University

2020

Abstract

In this research, a wire and arc additive manufacturing process for superalloy Hastelloy X was developed and the resulting material was characterized. The effects of parameters in the TIG based process were investigated for single layer samples using the Taguchi method and an analysis of variance (ANOVA). Multi-layer deposition strategies were also tested and no significant difference was found between printing layers in the same direction or in alternating directions. Due to the excessive heat input of the preliminary trials, three distinct zones were identified and characterized by the size and distribution of the molybdenum carbides within the matrix grain formations. By refining deposition strategies and process parameters, the resulting multi-layer samples exhibited less variation in the size and shape of the molybdenum carbides. Hardness testing confirmed that there is little to no variation in hardness along or across the print direction, suggesting a constant thermal history throughout. Finally, the isothermal oxidation behavior of AM Hastelloy X was compared to the wrought alloy through testing in air at 1080°C. The parabolic oxidation rate constant, k_1 , of the AM samples was determined to be $4.54 \times 10^{-8} \text{ g}^2/\text{cm}^4/\text{h}$. Results suggest that the AM samples may have an advantage in oxidation resistance due to finer grains and perhaps a better composition uniformity. However, weight gains between the wrought and AM samples were quite similar suggesting an equivalent oxidation behavior.

Acknowledgements

I would like to take this opportunity to express my gratitude to those who have helped me throughout the completion of my degree at Carleton University.

First and foremost, I would first like to thank my thesis co-supervisors, Dr. Xiao Huang and Dr. Jeremy Laliberté, for their guidance and support. Their combined expertise, their support, and their patience allowed me to conduct my research and complete this process.

I would also like to thank all my friends and family members for their continuous encouragement throughout this process. Finally, I would like to thank my parents for their endless love and support during this process.

Table of Contents

Abstract.....	iii
Acknowledgements	iv
Table of Contents	v
List of Tables	viii
List of Figures.....	ix
Chapter 1: Introduction	1
1.1 Motivation	1
1.2 Objectives.....	1
1.3 Thesis Overview.....	2
Chapter 2: Background Information and Literature Review	4
2.1 Additive Manufacturing	4
2.1.1 Introduction to Additive Manufacturing	4
2.1.2 Directed Energy Deposition Processes	9
2.1.3 Applications	13
2.2 Arc Welding	16
2.2.1 Gas Tungsten Arc Welding (GTAW)	16
2.2.2 Gas Metal Arc Welding (GMAW).....	18
2.2.3 Plasma Arc Welding (PAW).....	19
2.3 Additive Manufacturing Materials	21
2.3.1 Feedstock Material.....	21
2.3.1.1 Powder.....	21
2.3.1.2 Wire	22
2.3.2 AM Material Properties.....	23

2.4	Design of Experiments	27
2.4.1	Taguchi Method	28
2.5	Superalloys	30
2.5.1	Hastelloy X	33
2.6	Oxidation of Superalloys.....	34
2.6.1	Oxidation Mechanisms.....	35
2.6.2	Oxidation Rates.....	36
2.6.3	Types of Oxidation in Nickel-Based Superalloys	39
Chapter 3: Experimental Procedure		40
3.1	Directed Energy Deposition Machine	40
3.2	Material Selection.....	41
3.3	Study of Effects of Process Parameters.....	42
3.4	Sample Preparation.....	45
3.5	Isothermal Oxidation Testing	47
3.6	Hardness Testing	48
3.7	Wear Test.....	48
3.8	SEM and EDS Analysis.....	51
Chapter 4: Results and Discussion		53
4.1	Effects of Process Parameters.....	53
4.1.1	Analysis of Variance (ANOVA).....	61
4.2	Multi-layered Samples.....	63
4.2.1	Preliminary Trials.....	64
4.2.2	Final Results of Multi-Layer Samples	70
4.3	Isothermal Oxidation Testing	74

Chapter 5: Concluding Remarks and Future Work	83
5.1 Effects of WAAM Process Parameters	83
5.2 Multi-layered Samples.....	84
5.3 Isothermal Oxidation Testing	85
References.....	87

List of Tables

Table 1: L ₉ (3 ⁴) orthogonal array	30
Table 2: L ₁₆ (4 ⁴) orthogonal array.....	30
Table 3: Nominal composition of Hastelloy X alloy [64].	34
Table 4: Experimental factors and levels.....	43
Table 5: Experimental L ₁₆ (4 ⁴) orthogonal array.	44
Table 6: Process parameters used for multi-layer samples (B41, B42, and B43)	67
Table 7: Final process parameters used for multi-layer samples	70

List of Figures

Figure 1: Comparison of conventional manufacturing (CM) and additive manufacturing (AM). A) Subtractive manufacturing, B) formative manufacturing, and C) additive manufacturing.	5
Figure 2: Metallic additive manufacturing methods. A) Powder bed fusion (PBF), B) sheet lamination, and C) directed energy deposition (DED).	7
Figure 3: Comparison of multi-material AM and multi-material functionally graded AM [12].	10
Figure 4: Examples of WAAM implemented using various types of robotic control systems. A) ABB welding robot [14], B) retrofitted friction stir welding machine [14], C) retrofitted milling machine [21], and D) enclosed ABB welding robot [22], and E) custom built machine.	13
Figure 5: GE sensor housing for a high-pressure compressor (A) [24] and fuel nozzle (B) [25].	14
Figure 6: FAA certified Ti64 component for the Boeing 787 [26].	15
Figure 7: Lockheed Martin fuel tank dome produced using Sciaky EBAM technology [27].	16
Figure 8: Illustration of the gas tungsten arc welding (GTAW) process [28].	17
Figure 9: Illustration of the gas metal arc welding (GMAW) process [28].	18
Figure 10: Illustration of the plasma arc welding (PAW) process [28].	20
Figure 11: Likelihood of WAAM process defects in various materials [39].	24
Figure 12: Example of setup required for high pressure rolling of WAAM components [41].	25

Figure 13: Turbine blades for with (a) equiaxed, (b) columnar, and (c) single crystal grain structures [57].	32
Figure 14: Transportation mechanisms and interface reactions of metal oxidation. a) cation mobile b) anion mobile [69].	36
Figure 15: Different relationships for oxidation kinetics of metals [72].	37
Figure 16: Wire-based directed energy deposition machine.	41
Figure 17: Sample geometry measurements in SEM A) height, B) width, C) wetting angle, and D) melt through depth.	44
Figure 18: Progression of machining for sample preparation.	46
Figure 19: Position and direction of hardness measurements taken on additively manufactured specimens.	48
Figure 20: Pin-on-disk tribometer used for wear testing.	49
Figure 21: Sample wear test data.	50
Figure 22: Sample wear track (A) and wear scar on ball bearing (B).	50
Figure 23: Averaged wear track profile.	51
Figure 24: Tescan Vega II XMU-SEM used for analysis.	52
Figure 25: Top view of single layer weld beads.	54
Figure 26: Low oblique angle view of single layer weld beads.	55
Figure 27: SEM images showing bead and substrate microstructure (Sample B10).	56
Figure 28: Voids at the bead-substrate interface (Bead shown on top).	58
Figure 29: Elemental scan results across bead-substrate interface (Bead shown on left).	59
Figure 30: Quantitative EDS analysis across bead-substrate interface (oriented in same direction as labeled in Figure 29).	59

Figure 31: Composite plot of EDS scans (10 point moving averages) across bead-substrate interface (oriented in same direction as labeled in Figure 29).....	60
Figure 32: Molybdenum carbides present in bead material.....	60
Figure 33: Interval plots displaying significant trends between factors and responses....	62
Figure 34: Interval plots displaying significant trends between factors and responses....	63
Figure 35: Three layered specimens used to compare printing strategies. Each specimen shown in two views: top view (top) and low oblique angle view (bottom).....	65
Figure 36: Multiple layer specimens shown in two views with cross sections on the right.	68
Figure 37: Microstructure of specimen B43 from bottom to top of cross section.....	69
Figure 38: Sample of typical multi-layered specimen.	71
Figure 39: Cross sectional microscopy of AM sample.....	72
Figure 40: Hardness testing along build direction of AM specimen.	74
Figure 41: $(\text{Mass change/area})^2$ vs time for isothermal oxidation of Hastelloy X at 1080°C.	75
Figure 42: SEM imaging of surface oxide thickness after A) 5 hours, B) 100 hours, C) 500 hours, and D) 1000 hours.....	77
Figure 43: Oxide thickness vs time for isothermal oxidation of Hastelloy X at 1080°C.	78
Figure 44: Example of spallation present on 1000-hour specimens.	79
Figure 45: Quantitative EDS analysis across the oxide-substrate interface of an AM sample after 500 hours (oxygen omitted).....	80
Figure 46: Quantitative EDS analysis across the oxide-substrate interface of a wrought sample after 500 hours (oxygen omitted).	80

Figure 47: Detailed view of metal-oxide interface after 1000 hours of oxidation test. 81

Figure 48: Location of spallation in wrought sample after 500 hours. 82

Chapter 1: Introduction

This chapter includes the motivations and objectives of the work performed as well as an overview of each chapter.

1.1 Motivation

The potential to reduce material waste, lower part costs, decrease lead times, and improve production times has made additive manufacturing a desirable design and manufacturing tool for many industries. Wire and arc additive manufacturing is particularly well suited for gas turbine, tooling, heavy industry, and space applications. For the successful adoption of this relatively new technology, first the process itself must be developed and characterized. This includes developing an understanding of the effects of process parameters as well as deposition strategies on the resulting geometry and microstructure. Additionally, differences in microstructure and mechanical properties between AM and wrought materials must be considered in the engineering design process of AM components.

1.2 Objectives

The purpose of this thesis is to present the development and characterization of an additive manufacturing process for superalloy Hastelloy X and to compare the oxidation behavior to wrought Hastelloy X.

1.3 Thesis Overview

This thesis is organized into five chapters; a description of each chapter is provided in this section.

Chapter 1: Introduction – The motivations and objectives of the work performed as well as an overview of each chapter is provided.

Chapter 2: Background Information and Literature Review – This chapter is intended to provide the reader with an introduction to the information relevant to the topics covered in this thesis including: additive manufacturing (AM) processes, arc welding, AM material properties, superalloys, and oxidation behavior.

Chapter 3: Experimental Procedure – This chapter details the additive manufacturing setup including both the wire and arc additive manufacturing (WAAM) machine and materials used. Experimental strategies used to study the effects of process parameters are described. Furthermore, sample preparation and testing methods are discussed.

Chapter 4: Results and Discussion – The effects of process parameters in TIG based WAAM for single layer Hastelloy X alloy samples are summarized and discussed along with an analysis of variance (ANOVA). Deposition strategies for multi-layer samples are also discussed. Finally, the isothermal oxidation behavior of Hastelloy X is compared between the additively manufactured specimens and conventional wrought material.

Chapter 5: Concluding Remarks and Future Work – This chapter summarizes the work completed to date related to the development and characterization of the WAAM process of superalloy Hastelloy X and proposes future work to expand upon the research.

Chapter 2: Background Information and Literature Review

This chapter includes an overview of the information relevant to the topics covered in this thesis, including additive manufacturing (AM) processes, arc welding, AM material properties, superalloys, and oxidation.

2.1 Additive Manufacturing

Demand for advanced manufacturing techniques, intricate designs, and material performance has allowed additive manufacturing (AM) to become an increasingly useful technology for a range of industries [1], [2]. AM has gained attention due to the numerous benefits it provides including reduced material waste, lower part cost, shorter lead times, and faster production times [3], [4]. AM can be implemented with metals, polymers, or ceramics and allows for complex components to be designed and fabricated which would otherwise not be possible using conventional manufacturing methods.

2.1.1 Introduction to Additive Manufacturing

AM is a manufacturing process where three-dimensional parts are formed by depositing and joining material layer-by-layer in an additive manner. AM contrasts conventional manufacturing (CM) methods utilizing subtractive or formative manufacturing approaches. The difference between AM methods and CM methods is illustrated in Figure 1.

Subtractive manufacturing begins with a block of material of which material is removed to create a final shape by several machining passes. Inherently this process creates significant material waste which cannot always be recycled. Additionally, there are costs associated

with tool wear and machining time. For difficult to machine alloys, such as superalloys, these costs can be significant.

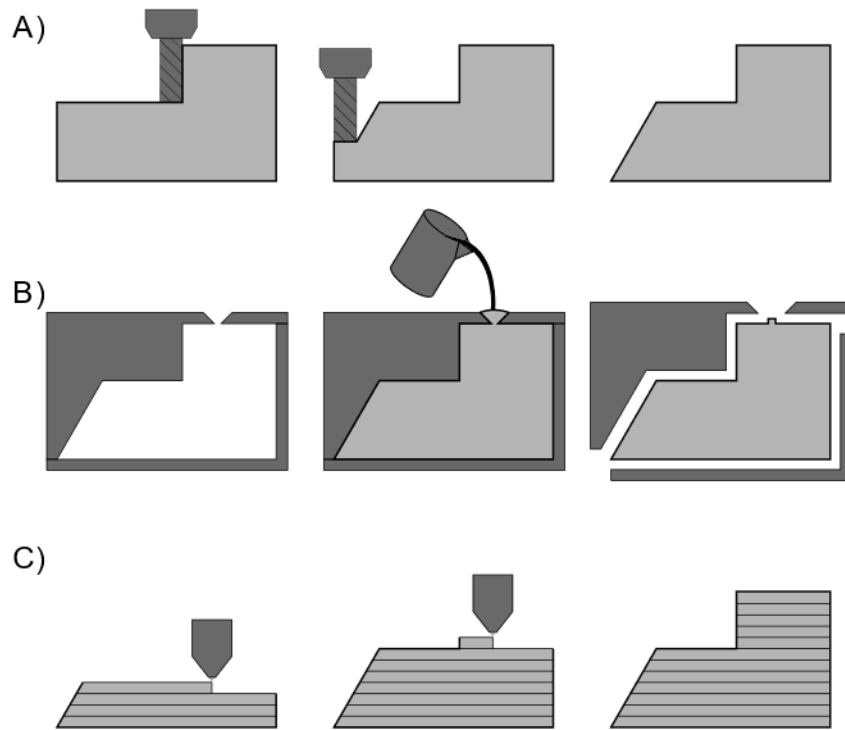


Figure 1: Comparison of conventional manufacturing (CM) and additive manufacturing (AM).

A) Subtractive manufacturing, B) formative manufacturing, and C) additive manufacturing.

Formative manufacturing is a general term describing processes such as injection molding, die casting, pressing, etc. Components created from formative manufacturing produce less material waste than subtractive manufacturing however typically require additional machining or grinding to reach the desired surface finish. In most formative manufacturing processes, expensive molds or dies are required. Since these tools are unique to each

manufactured part, formative manufacturing is usually only economical at high scale productions. The tools also experience wear and require refurbishment or replacement after some amount of use. Advanced casting techniques allow for complex geometries, such as internal cavities, that would not be possible with any other conventional manufacturing techniques. Additionally, casting processes can be used to create directionally solidified or single crystal microstructures for superalloy gas turbine blades [5].

Additive manufacturing creates parts in a net shape or near net shape condition by depositing material layer by layer allowing for complex geometries to be created that would otherwise not be possible using conventional manufacturing methods. AM was originally considered most useful for rapid prototyping. Advances in AM technology has facilitated a shift from rapid prototyping to the manufacturing of production components. Importantly for the industry, AM can reduce part costs as well as lead times for replacement or production components granting manufacturers more flexibility in their supply chain, particularly for job shop environments.

In the aerospace industry, the so called “buy-to-fly ratio” is used to quantify the relative amount of waste generated during part production. The buy-to-fly ratio is the ratio between the amount of raw material used and the material used in the final part. Although rarely possible, the optimal buy-to-fly ratio could approach 1, meaning that no material was wasted during part production. Reducing the buy-to-fly ratio is particularly advantageous in the aerospace industry for hard-to-machine and costly materials such as titanium or nickel superalloys. Subtractive manufacturing processes will inherently have the highest

buy-to-fly ratio as a significant amount of material must be removed from the initial block of material. Formative and additive manufacturing methods both produce near net-shape parts meaning minimal machining is required and a low buy-to-fly ratio can be achieved.

According to ISO/ASTM 52900:2015, a standard defining additive manufacturing terminology, all metallic AM processes are classified into three categories; powder bed fusion (PBF), sheet lamination, and directed energy deposition (DED) [6]. The different processes are illustrated in Figure 2. The AM processes differ in terms of material feedstock type, material deposition method, and energy source.

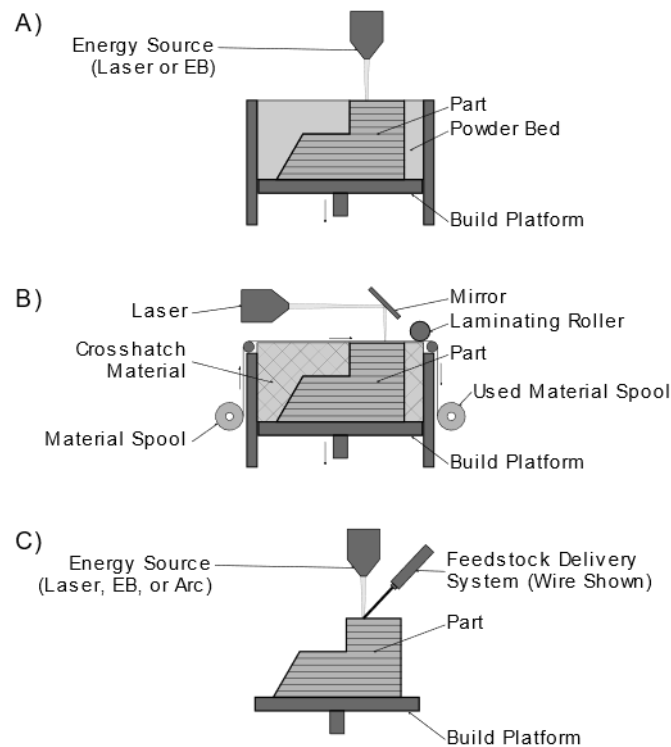


Figure 2: Metallic additive manufacturing methods. A) Powder bed fusion (PBF), B) sheet lamination, and C) directed energy deposition (DED).

In powder bed fusion (PBF) processes, a thin layer of powder material is deposited over the entire surface of the build platform. The exposed powder is selectively fused using a concentrated energy source to form the cross section of that layer. Once the powder is fused, an additional layer of powder is deposited on top and the process is repeated until the part is formed [7]. PBF processes typically provide the highest detail resolution and require no support structures [8]. Unused powder in the print volume must be filtered or recycled before being reused to eliminate any contamination, moisture absorption, oxidation, and remove any partially fused particles [9], [10]. The extra steps required to reuse powder adds a significant operational cost to PBF processes.

Sheet lamination is a process where sheets are selectively bonded or fused together to form the part's cross section before being cut out from the sheet. After bonding each layer, a laser will follow the outline of the cross section to cut the bonded section free. This process is then repeated with an unused section of sheet material until the part is formed [7]. Typically, for metallic sheet lamination processes, ultrasonic welding is used to bond each layer allowing for the use of dissimilar metals in a single part [11]. Additionally, sensor or fibers can be embedded into the structure. Since each layer creates waste at least equal to the size of the build platform, the process produces a significant amount of waste for small parts.

The third and final category of metallic AM processes is called directed energy deposition where material is deposited and fused directly onto the part using a form of focused thermal energy [7]. In DED processes, the energy source and material feeder are typically mounted

on a single print head which follows the print path. Directed energy deposition processes can use an electron beam, a laser, or an electric arc as its energy source with either wire or powder feedstock material. DED processes are further discussed in Section 2.1.2.

Applications for sheet lamination processes are limited and therefore most metallic AM is performed using either PBF or DED. These categories include several different processes that vary in feedstock form and energy source. PBF uses a laser or an electron beam as the energy source and includes selective laser sintering (SLS), selective heat sintering (SHS), selective laser melting (SLM), direct metal laser sintering (DMLS), and electron beam melting (EBM). DED includes processes such as laser engineered net shaping (LENS), laser metal deposition (LMD), direct metal deposition (DMD), electron beam additive manufacturing (EBAM), electron beam freeform fabrication (EBFFF), and wire and arc additive manufacturing (WAAM).

2.1.2 Directed Energy Deposition Processes

Directed energy deposition processes deposit and fuse material directly onto the part using a form of focused thermal energy. DED processes can use either wire (e.g. wire and arc additive manufacturing) or powder feedstock material.

In wire-based systems, a wire feed assembly is used to deliver the wire feedstock to the molten pool. Typically, a wire feed assembly uses several drive rollers and may include a wire straightener to remove cast and helix from the wire. Cast and helix result from wire spooling and can negatively affect the positional accuracy of the material feed system.

In powder-based systems, powder is stored in a reservoir or hopped and carried through a series of pipes to the nozzle using a carrier gas. Powder feedstock can also be transported using gravity or mechanical means such as a worm gear. Due to the nature of the powder delivery system, some of the powder exiting the nozzle will not fuse to the part. Powder capture efficiency, expressed as a percentage, is used to quantify the amount of material ejected through the nozzle compared to the amount of material that is fused to the part. The powder capture efficiency of current DED systems is typically less than 50% [10].

In both powder- and wire- based systems, multiple material feeders can be used simultaneously. With different alloys in each material feeder, functionally graded materials are possible. Functionally graded materials allow for material properties such as strength or toughness to be tailored locally per the requirements of the part [12]. Figure 3 illustrates a comparison between multiple-material additive manufacturing (MMAM) and multiple-material functionally graded additive manufacturing (MM FGAM).

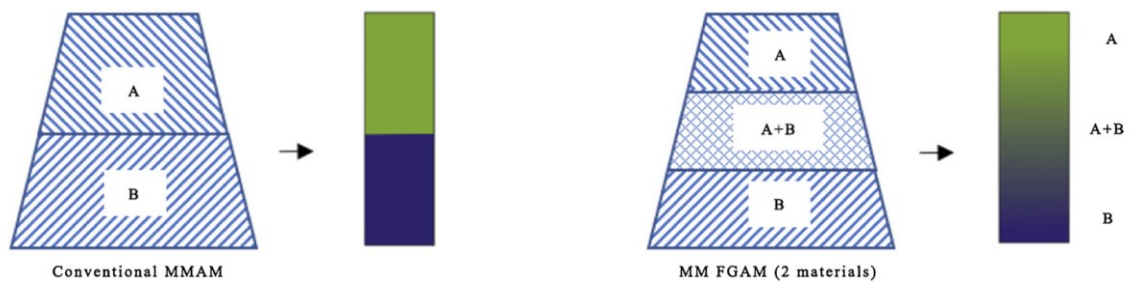


Figure 3: Comparison of multi-material AM and multi-material functionally graded AM [12].

DED systems can use a number of different types of energy sources including electron beam [13], electric arc [14], or laser [15]. The type of energy source affects the operational requirements, potential applications, and complexity of the DED system.

Electron beam (EB) systems require the entire build volume to be enclosed in a vacuum during operation [13]. This significantly increases the operational costs and process time of EB AM as opposed to systems that require only an inert environment or a flow of shielding gas. Additionally, the vacuum can cause evaporation of particularly volatile elements from the molten pool resulting in a difference in composition between the feedstock material and the finished part [16]. EB systems generally have the highest efficiency and largest standoff distance compared to laser and electric arc systems. A larger standoff distance, of up to 3 m, reduces the possibility of contamination or damage occurring to the energy source.

Currently there are several options for laser beam energy source available for additive manufacturing including Yb-fiber lasers, CO₂ lasers, Nd:YAG lasers, and excimer lasers [17]. When selecting a laser type, it is important to consider power density, wavelength, spot size, and the method of beam delivery (i.e. fiber delivery or optical delivery). Most laser metallic AM machines use either CO₂ lasers or Nd:YAG lasers as an energy source [17]. To optimize the process, engineers must consider various process parameters including spot size, scan speed, and power output as well as the coupling efficiency which is a function of the wavelength and selected material. Generally, laser-based systems provide the highest detail resolution of all energy sources.

As an energy source, electric arcs require the lowest capital investment due to the simplicity of the equipment and the prevalence of the technology in the welding industry. Metallic additive manufacturing can be accomplished with various electric arc energy sources including gas metal arc welding (GMAW) [18], gas tungsten arc welding (GTAW) [19], and plasma arc welding (PAW) [20]. Arc based systems operate with a high efficiency and can accommodate a range of deposition rates and heat inputs. Material deposition can also be further manipulated by pulsing the arc and by altering the waveform and frequency. These techniques can be used to reduce heat input and thus reduce residual stress and distortion which typically occur in arc-based AM. These systems can be constructed as a stand-alone commercial unit or assembled from commercially available components including a computer controlled robotic system, a welding power source, a welding torch, and a wire feed system. Several examples of WAAM systems created for research environments are shown in Figure 4. The research conducted for this thesis was conducted using the custom build machine shown in Figure 4 E) which cost less than \$10,000 while commercially available laser or EB systems typically cost around \$1M.

Typically, DED systems are used for low volume production, rapid prototyping, or repair purposes. Since the DED process deposits and fuses material directly to the part and does not require the build platform to remain horizontal, the systems often incorporate 5 or more axes of motion. This makes DED systems particularly well suited for repair purposes as material can be deposited and fused onto an existing part. The additional axes of rotation allow the part to be manipulated such that the molten pool remains horizontal and the effect of gravity are negated.

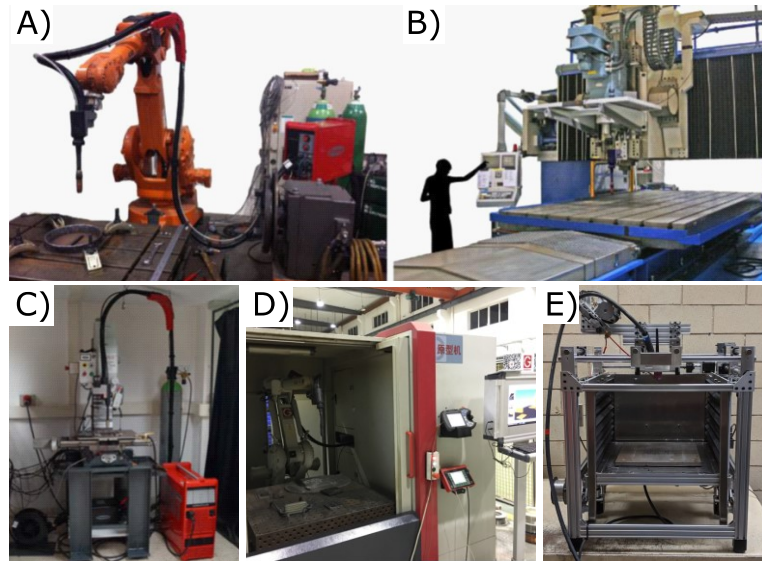


Figure 4: Examples of WAAM implemented using various types of robotic control systems.

A) ABB welding robot [14], B) retrofitted friction stir welding machine [14], C) retrofitted milling machine [21], and D) enclosed ABB welding robot [22], and E) custom built machine.

2.1.3 Applications

Since its inception, additive manufacturing has been a focus of the aerospace industry as a means to reduce lead times and enable complex designs and geometries for new components. However, in the aerospace industry, regulatory requirements add a significant cost to the development of AM parts in terms of rigorous material testing and process qualification to ensure robust performance. There are currently numerous efforts by regulators and standards organizations to develop clear guidelines for the qualification process. This also includes the ASTM F42 committee on additive manufacturing which develops standards to encourage research and implementation of AM [23]. ASTM currently has standards on the topics of AM materials and processes, design, terminology, and test methods.

The first commercial jet engine AM component to be qualified by the Federal Aviation Administration (FAA) was produced by GE [24]. In early 2015, the FAA qualified a temperature sensor housing to be flown in the high-pressure compressor stage of the GE90-94B jet engine. The sensor housing, shown in Figure 5, was manufactured using PBF and flown on Boeing 777 aircraft. Also shown in Figure 5 is an additively manufactured fuel nozzle produced by GE using PBF [25].

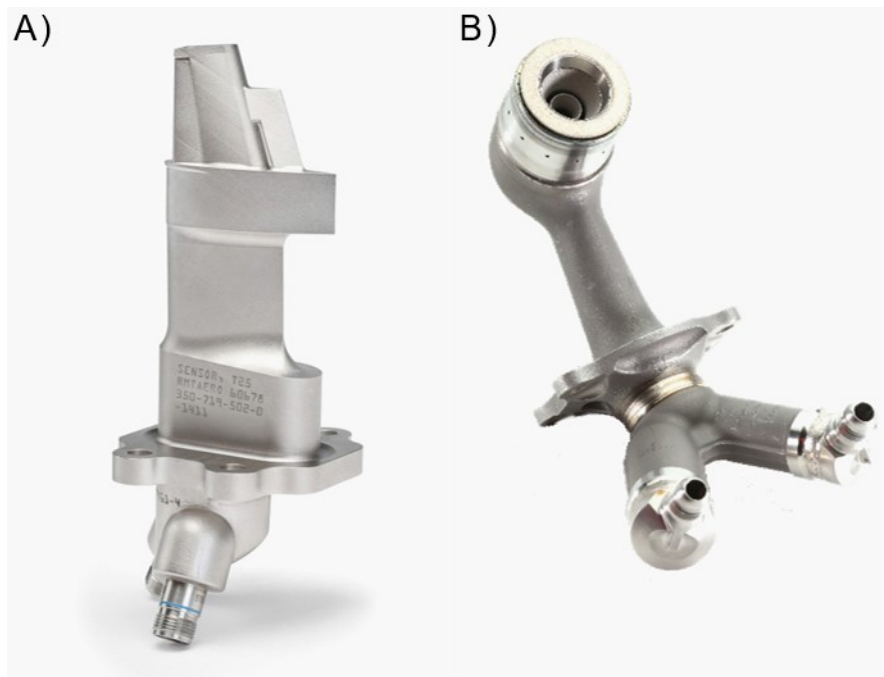


Figure 5: GE sensor housing for a high-pressure compressor (A) [24] and fuel nozzle (B) [25].

Although the GE sensor housing and fuel nozzle are examples of non-critical and non-structural component, the industry has long been focused on developing AM technologies to allow for the production and certification of structural and critical aircraft components. Boeing was the first to fly with a structural AM part qualified by the FAA [26]. Boeing

partnered with Norsk Titanium to manufacture the Ti-6Al-4V component, shown in Figure 6, using its Rapid Plasma Deposition (RPD) technology.



Figure 6: FAA certified Ti64 component for the Boeing 787 [26].

Additive manufacturing has also been qualified for space applications by Lockheed Martin Space and Sciaky Inc. Using the Sciaky Electron Beam Additive Manufacturing (EBAM) process, they were able to produce 46-inch diameter domes, shown in Figure 7, for use on the high-pressure fuel tanks of the LM 2100 satellite [27]. Qualified by NASA's performance and reliability requirements, the AM components will become a standard option on the satellites. By switching to AM, Lockheed Martin claims a reduction in production time of 87%, from two years to 3 months, and a significant decrease in material waste.



Figure 7: Lockheed Martin fuel tank dome produced using Sciaky EBAM technology [27].

2.2 Arc Welding

This section covers several common electric arc welding processes that can be used for additive manufacturing. In each of the following subsections, a process, named in accordance to standard American Welding Society (AWS) terminology, is described. AWS terminology is used to avoid the use of industry specific naming. Arc welding processes including any welding process where energy is generated by an electric arc.

2.2.1 Gas Tungsten Arc Welding (GTAW)

In the gas tungsten arc welding (GTAW) process, a non-consumable tungsten electrode is used to form an arc between the electrode and the work. The GTAW process is shown in Figure 8. A shielding gas is required to protect the molten metal from foreign

contamination and oxidation while cooling. The shielding gas is supplied through the welding torch to completely cover the molten pool and the electrode. Typically, an inert shielding gas is used such as argon or helium. GTAW is relatively inexpensive due to the low-cost equipment yet it is capable of high-quality welds with few defects. GTAW allows for manual or automated feeding of filler material. However, for AM processes the feedstock material will always be fed automatically.

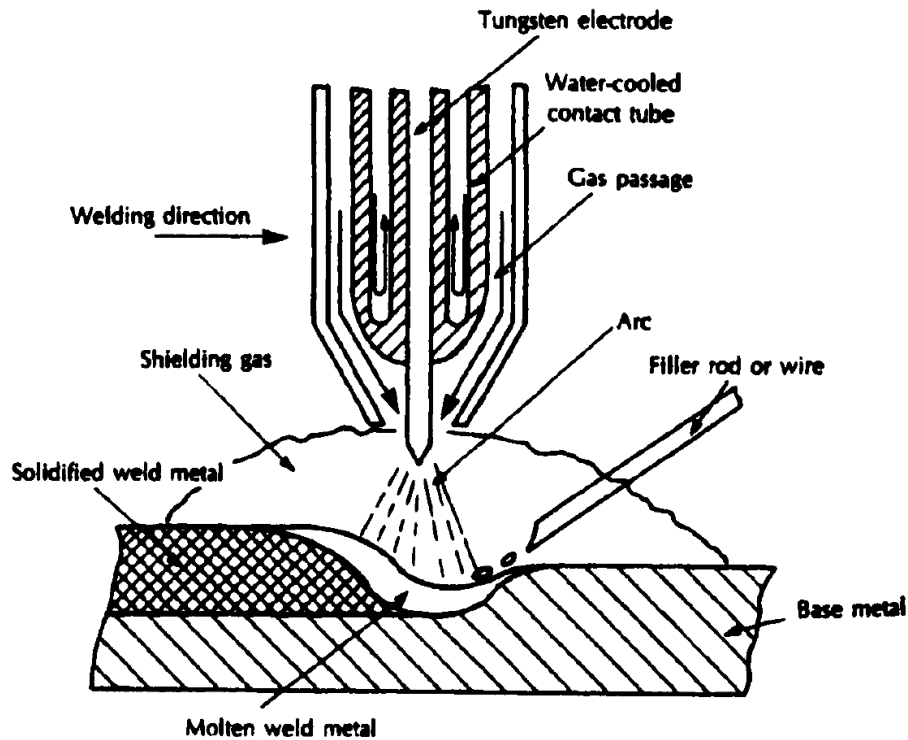


Figure 8: Illustration of the gas tungsten arc welding (GTAW) process [28].

Some of the GTAW process parameters that must be considered include arc current, arc voltage, travel speed, wire feed rate, shielding gas type, shielding gas flow rate, arc length,

electrode diameter, and electrode tip angle. Empirical models have been created to relate these process parameters with bead geometry in GTAW applications [29]–[31].

2.2.2 Gas Metal Arc Welding (GMAW)

Gas metal arc welding (GMAW) uses a continuous consumable electrode to form the arc between the torch and the work, as shown in Figure 9. Like GTAW, shielding gas is required to protect the molten metal and is supplied through the welding torch.

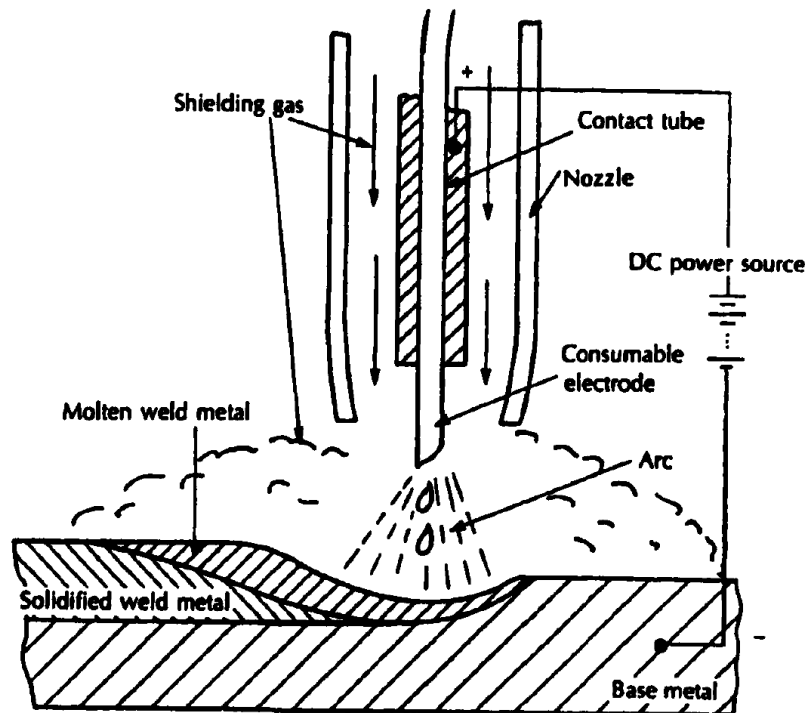


Figure 9: Illustration of the gas metal arc welding (GMAW) process [28].

In GMAW, an arc is formed between a continuous consumable electrode and the work to melt both the base metal and the electrode itself. The behavior of the material deposition,

or metal transfer mode, varies significantly depending on the amount of current supplied. There are three metal transfer modes commonly associated with GMAW; short circuit transfer, globular transfer, and spray transfer. For short circuit transfer, the electrode contacts the weld pool multiple times per second to deposit material. This transfer mode requires the lowest amount of input current and uses the smallest electrode diameter. Since such a small current is applied to the work, the weld pool can cool more quickly making the process ideal for welding thin sections and bridging gaps. Globular transfer requires a slightly higher current to melt the electrode until a droplet, larger in diameter than the electrode, is formed and eventually drops onto the work. Typically, globular transfer requires the workpiece to remain horizontal as the weld pool and droplet are affected by gravity. The final metal transfer mode, spray transfer, requires a relatively high current that is above a certain minimum transition current. The process produces a stable and spatter-free transfer of material however since a large weld pool is formed, the work must remain horizontal to avoid negative effects of gravity. A study of GMAW arc modes and their effects on mechanical properties found that at a constant deposition rate modes with lower heat input produce greater tensile strength and hardness [32]. For this reason, most of the GMAW AM work to date has been conducted using short circuit transfer mode, also known as cold metal transfer (CMT) [22], [33], [34].

2.2.3 Plasma Arc Welding (PAW)

Plasma arc welding is similar to GTAW except that the non-consumable electrode is concealed entirely within the torch and hot ionized gas is forced through a nozzle to constrict the arc. This process results in a higher energy density and the cylindrical arc

allows for variation in standoff distance. The higher energy density of PAW results in a deeper penetration and a significantly smaller heat affected zone (HAZ) than GTAW, however the equipment is more expensive. PAW is inherently more complicated than GTAW as the additional nozzle and orifice gas introduces new process parameters such as orifice diameter, orifice gas type, and orifice gas flow rate.

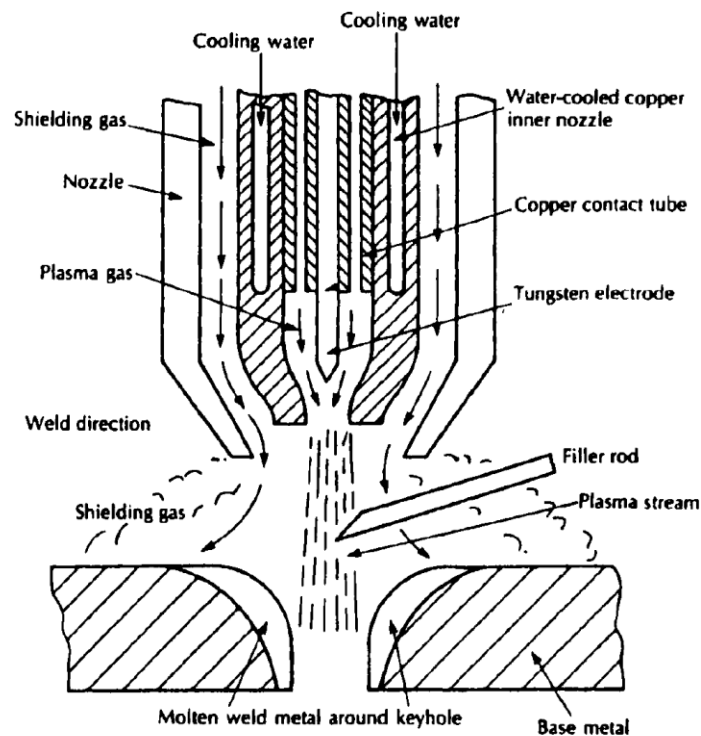


Figure 10: Illustration of the plasma arc welding (PAW) process [28].

In PAW, the arc can either be formed between the electrode and the work piece or between the electrode and the constricting nozzle known as a transferred arc or a non-transferred arc respectively. A transferred arc delivers heat to the weld pool from the anode spot as well as the high energy plasma jet whereas a non-transferred arc only delivers heat from

20

the plasma jet. Typically, non-transferred arcs are only used when it is undesirable or not possible to include the substrate in the circuit. Microstructural and mechanical properties have been investigated for both continuous and pulsed plasma arc additive manufacturing [35]–[37].

2.3 Additive Manufacturing Materials

This section discusses the topic of additive manufacturing materials with a focus on directed energy deposition systems.

2.3.1 Feedstock Material

In DED processes, either wire or powder feedstock material can be used. This section discusses the advantages and disadvantages of each.

2.3.1.1 Powder

As mentioned in Section 2.1.2, powder-based DED systems require a carrier gas to blow powder through a nozzle to be deposited onto the part using an energy source such as a laser. Blown powder inherently results in a stochastic distribution of material, therefore detail resolution and dimensional accuracy suffer compared to PBF processes. However, due to the fine powder size, powder-based DED systems perform better than the wire-based alternatives with respect to detail resolution, surface finish, and dimensional tolerance. Additionally, any blown powder not fused to the part must be collected and filtered in order to be reused.

To meet certification requirements, metallic additive manufacturing powder must be within a certain powder size distribution and must be free of contamination and oxidation. Typically, AM powders are produced using a gas atomization process. Due to these requirements, the raw material costs for powder-based AM are typically quite high compared to wire-based systems [14], [15], [38]. Additionally, metallic powders introduce a number of health and safety concerns to machine operators as well as the environment.

2.3.1.2 Wire

Wire feedstock delivery systems are much simpler than powder-based alternatives and require only a simple wire feeder. Wire feeders are commercially available for GMAW as well as automated welding process and typically use two or more drive wheels to deliver the material from the spool to the molten pool. Unlike powder deposition, wire deposition does not waste any material during the deposition process due to the focused and localized melting and deposition. However, wire-based systems sacrifice detail resolution and surface finish, meaning they can only produce near net shape parts. Additional machining steps are often required to achieve a finished part, therefore introducing some material waste to the process.

Wire feedstock is safer than powder materials and can easily be handled by operators. Additionally, wire feedstock is cheaper than powder feedstock for relatively ductile materials and a wider range of materials are available for additive manufacturing

applications due to the widespread use of wires for different types of welding. While wire based systems can achieve a higher deposition rate, typically the detail resolution suffers.

2.3.2 AM Material Properties

Academic institutions and the aerospace industry have developed metallic alloys for additive manufacturing capable of matching or exceeding the performance of traditional alloys. The deposition process of AM presents additional challenges compared to conventional manufacturing methods and an increased likelihood of defects. Typical defects from additive manufacturing processes include lack of fusion between layers, porosity and voids, cracks, distortion, and residual stress. Additionally, for powder-based AM processes it can be challenging to ensure compositional homogeneity. This section discusses material defects typically encountered in WAAM applications.

Figure 11 shows the relationships between various defects that may occur during WAAM processes of different materials. It should be noted that of all WAAM materials, titanium and nickel alloys are least likely to suffer defects while aluminum and bimetal alloys are most likely to suffer defects.

Due to the significant heat input and repeated heating and cooling cycles, the WAAM process experiences significant distortion and residual stresses in finished parts. Although WAAM parts are typically near net shaped, they often require additional machining, as excessive distortion can bring parts outside of geometric tolerances or cause improper alignment during the deposition of subsequent layers. Additionally, residual stress reduces

the fatigue performance and fracture resistance of a part [39]. For these reasons, reducing distortion and residual stress has been a significant area of research. It has been shown that distortion can be eliminated and residual stress significantly reduced by using a high pressure roller between each layer, as shown in Figure 12 [40]. Alternatively, optimization of process parameters or path planning can reduce residual stresses [41], [42]. In order to reduce residual stress and achieve the desired material strength, ductility, and hardness, post additive manufacturing heat treatment may also be employed.

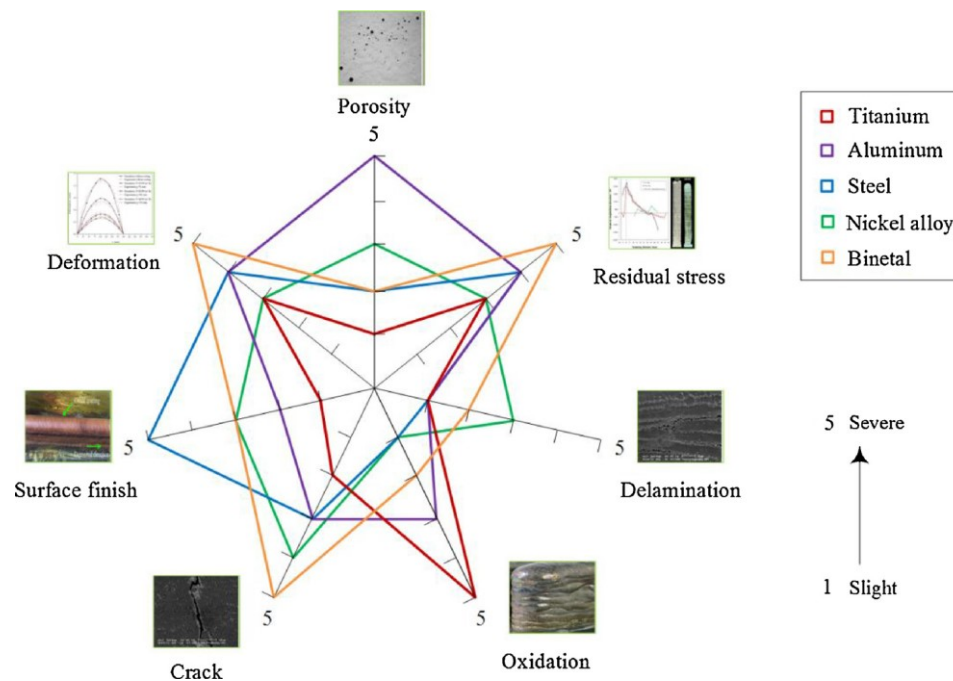


Figure 11: Likelihood of WAAM process defects in various materials [43].

Similar to conventional welding processes, porosity is a common defect resulting from WAAM. Porosity occurs as dissolved gases in the molten pool are entrapped during the solidification process. Porosity can reduce both strength and fatigue performance of welded

structures [44]. Of all AM materials, aluminum is the alloy most susceptible to porosity during the deposition process. Porosity in aluminum occurs because the solubility of hydrogen in aluminum increases by nearly 20 times as the metal is melted [45]. Sources of hydrogen during welding processes include dissociation of water, dissolved hydrogen in the base metal or filler wire, and contamination of shielding gas [46]. The likelihood of porosity can be reduced by thoroughly cleaning the substrate and wire as well as utilizing high purity shielding gases. Alternative methods have been investigated including inter-layer rolling, workpiece vibration, and cold metal transfer (GMAW only) [47]–[49].

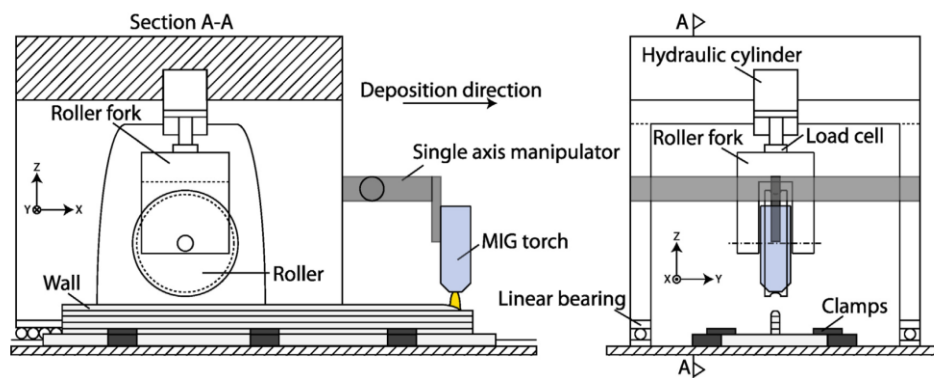


Figure 12: Example of setup required for high pressure rolling of WAAM components [40].

Some AM materials are prone to cracking during the cooling phase of the deposition process when residual tensile stress develops. The mechanism causing these cracks to occur is typically referred to as hot cracking and the likelihood of occurrence depends on how the alloy system solidifies as well as the cooling rate. Hot cracking occurs due to the difference in cooling rates of various alloying constituents which concentrates the lower melting point constituents at the grain boundaries [50]. Pure metals are not susceptible to

hot cracking as they contain only a single phase. Hot cracking can either be avoided by reducing the total heat input or reducing the cooling rate, both of which are achievable by altering process parameters and deposition paths. Delamination is another form of defect which closely resembles cracking. Delamination is a phenomenon that occurs when layers are not completely fused. Delamination can occur when the heat input is insufficient to melt enough of the previous layer resulting in a lack of fusion. Delamination is typically observable on the macroscopic scale and can be increased by the presence of residual stress [41].

In addition to the material defects previously listed, anisotropy of mechanical properties is considered a common drawback for additive manufacturing. Incomplete melting of previous layers and columnar grain formations are cited as being main contributing factors to anisotropy of mechanical properties in AM materials [51]. Anisotropy of mechanical properties such as tensile strength, fracture toughness, and fatigue life are compared in accordance to the designations of ISO/ASTM standards as shown in Figure 13 [52].

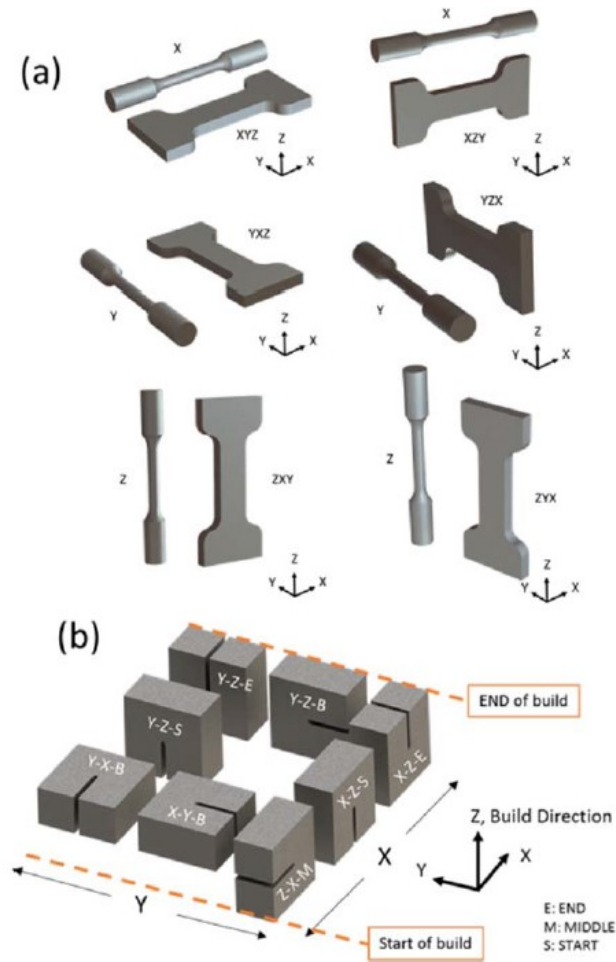


Figure 13: ISO/ASTM standard orientation designations for AM material testing [52].

2.4 Design of Experiments

In process engineering, formally designed experiments are used to determine relationships between input parameters and output performance. Since these processes can be complex in nature it is important that experiments are designed carefully to achieve reliable results. The designer of the experiment must note that not all input parameters have equal importance or influence on output performance.

For a given process there are many input parameters, also known as factors. Some factors are easily monitored and controlled whereas others can be difficult or costly to control. Experimental factors can therefore be classified as either controllable or uncontrollable. Although uncontrollable factors cannot be adjusted during the experiment, they may still influence output performance and should be considered by the designer. To ensure proper and complete analysis as well as reliable and meaningful results, design of experiments (DOE) should be implemented.

Design of experiments is a concept developed by Sir Ronald Fisher of the Rothamsted Agricultural Field Research Station London, England in the 1920's [53]. At the time, Fisher conducted a series of experiments to measure the effects of various factors on crop yields. DOE has since been adopted by several industries and disciplines as a process for planning, designing, and analyzing experiments to obtain reliable and meaningful conclusions. DOE can be applied to manufacturing or process engineering to improve yield, profits, and process capabilities as well as reducing costs and increasing the general understanding of important process parameters.

2.4.1 Taguchi Method

Although traditional DOE methods are still used to this day there are limitations related to the total number of experiments required and their associated costs as well as the reliability and repeatability of the results. By identifying these issues Dr. Genichi Taguchi developed new methodologies to increase the quality and reliability of engineering experimentation [54], [55].

Taguchi's general philosophy was that quality should be designed into products by developing robust manufacturing methods. Robustness in manufacturing means that the output quality is less sensitive to external factors such as operator error and environmental changes [56]. The Taguchi method uses a set of standardized tables called orthogonal arrays to define the test matrix for a given experiment. The orthogonal arrays define the experimental test matrix by a specifically determined combinations of factors and levels. For example, Table 1 shows an $L_9 (3^4)$ orthogonal array for an experiment of four factors with three levels each and

Table 2 show an $L_{16} (4^4)$ orthogonal array for an experiment of four factors with four levels each.

Table 1: $L_9 (3^4)$ orthogonal array

Run	Control factors and levels			
	A	B	C	D
1	1	1	1	1
2	1	2	2	2
3	1	3	3	3
4	2	1	2	3
5	2	2	3	1
6	2	3	1	2
7	3	1	3	2
8	3	2	1	3
9	3	3	2	1

Table 2: $L_{16} (4^4)$ orthogonal array.

Run	Control factors and levels			
	A	B	C	D
1	1	1	1	1
2	1	2	2	2
3	1	3	3	3
4	1	4	4	4
5	2	1	2	3
6	2	2	1	4
7	2	3	4	1
8	2	4	3	2
9	3	1	3	4
10	3	2	4	3
11	3	3	1	2
12	3	4	2	1
13	4	1	4	2
14	4	2	3	1
15	4	3	2	4
16	4	4	1	3

2.5 Superalloys

Superalloy is a term used to refer collectively to nickel-, cobalt-, and iron- based alloys used for high temperature applications. Superalloys are commonly used in gas turbine blades and rotors for both aerospace and power generation industries. Turbine blades are exposed to extremely high temperatures and stress, as such the development of creep and fatigue resistant alloys has been critical to improving gas turbine efficiencies.

Early iterations of gas turbine blades were forged from wrought nickel-based alloys. Nimonic alloys are examples of turbine blade materials developed in the 1940s [57]. As turbine inlet temperatures continue to increase in order to improve efficiency, additives such as aluminum and titanium were added to increase creep resistance however this also decreases the forgeability. The lack of forgeability and also the demand for single crystal alloys led to the development of cast nickel-based alloys for manufacturing of the airfoils.

The first cast turbine blades had the standard equiaxed grain structure of cast components, as shown in Figure 14. The next significant development came in the development of directionally solidified (DS) castings. Directional solidification eliminated transverse grain boundaries and significantly improved strength and creep resistance. Since the number of grain boundaries was decreased, some grain boundary strengtheners such as C, B, and Zr could be removed [58]. Grain boundaries are considered a point of weakness and they can act as a point for impurities to concentrate and lead to creep rupture. Single crystal (SC) casting pushed material limits further by eliminating grain boundaries entirely.

With the implementation of SC technology, the creep resistance of gas turbine blades was improved through the incremental developments in microstructures and alloying elements. In fact, throughout the first three generations there is a significant decrease in titanium (Ti) and molybdenum (Mo) concentrations and also an increased addition of rhenium (Re) as an alloying element [59]. Rhenium in nickel-based superalloys drastically improves creep life and is used in second and third generation superalloys. The composition of Rhenium by weight for the second and third generation alloys are around 3% and 6% respectively.

In the newer generation of SX alloys, ruthenium (Ru) is also added to improve segregation and reduce density.

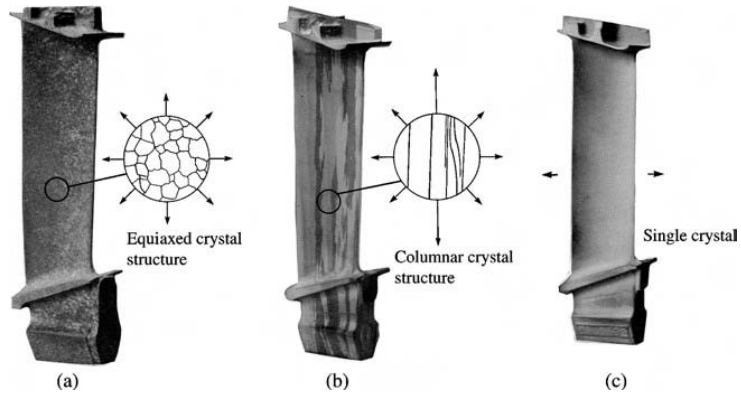


Figure 14: Turbine blades for with (a) equiaxed, (b) columnar, and (c) single crystal grain structures [60].

Nickel-based superalloys are known to be particularly difficult to machine compared to traditional alloys. Nickel-based superalloys are difficult to machine for several reasons including their high toughness, high strength of material at elevated temperatures, high degree of work hardening, and poor thermal conductivity [61]. Machining nickel-based superalloys requires special tooling and techniques that increase production times and costs [62]. Reducing the buy-to-fly ratio is therefore particularly advantageous for these superalloys, taking into consideration of material cost and process time, and can be achieved by using either formative or additive manufacturing methods to produce near net-shape parts requiring minimal machining.

Traditionally, gas turbine components such as blades and discs are joined either by welding or mechanical fasteners [63]. While mechanical fasteners, such as bolts, provide the

flexibility for repair and overhaul, it increases the part count and adds to the complexity of the assembly. Alternatively, welded assemblies are advantageous since they form a single component without any mechanical joints [64]. Welding gas turbine components generally limits material selection based on alloy weldability. Superalloys with high levels of alloying elements are often considered to have poor weldability as they are susceptible to hot cracking during solidification or strain-age cracking during heat treatment [65]. Poor machinability and limited weldability make superalloys most suitable for AM applications.

2.5.1 Hastelloy X

Hastelloy X is a solid solution strengthened nickel-based superalloy developed by HAYNES International primarily composed of nickel, chromium, iron, and molybdenum with solid solution strengthening from molybdenum, cobalt, and tungsten. Molybdenum carbides precipitates can be formed. The nominal composition is shown in Table 3.

Table 3: Nominal composition of Hastelloy X alloy [66].

	Weight %
Nickel	47 (Bal.)
Chromium	22
Iron	18
Molybdenum	9
Cobalt	1.5
Tungsten	0.6
Carbon	0.1
Manganese	1 (max)
Silicon	1 (max)
Boron	0.008 (max)
Niobium	0.5 (max)
Aluminum	0.5 (max)
Titanium	0.15 (max)

Hastelloy X possesses good oxidation resistance, formability, and high temperature performance [66]–[68]. In the aerospace industry, the nickel-based solid solution superalloy is typically used for ducts or liners in the combustion stage of gas turbine engines. Hastelloy X is considered to have excellent weldability with low likelihood of crack formation. Hastelloy X can be welded using GTAW or GMAW.

2.6 Oxidation of Superalloys

Oxidation is a corrosion process that occurs to metal alloys in gaseous environments and causes the formation of an oxide layer to form on the outer surface of the metal. Most metal materials are susceptible to oxidation at elevated temperatures, including superalloys commonly used in gas turbine applications. Oxidation can reduce the performance of superalloys by causing surface cracking, spallation, erosion, or depletion of alloying elements. The aerospace industry is heavily invested in increasing the oxidation resistance of gas turbine components primarily by developing new superalloys and thermal barrier

coatings (TBCs). The following sections discuss oxidation mechanisms, oxidation rates, and types of oxidation experienced by nickel-based superalloys.

2.6.1 Oxidation Mechanisms

The formation of an oxide layer on a metal M exposed to an oxygen rich gaseous environment is represented by the Equation 1.



The solid reactant product, MO, forms as a barrier between the two reactants. Therefore, for the reaction to continue, two half-reactions occur at the metal-oxide interface and the oxide-gas interface to form metal ions and oxygen ions respectively. There are several different mechanisms to explain the transport of ions through the oxide scale that depend on the stoichiometric or non-stoichiometric nature of the oxide [69]. In practice, all compounds display a combination stoichiometric and non-stoichiometric crystals often dominated by one or the other.

In most cases, the metal ions or oxygen ions are transported across the oxide layer through the presence of defects. The oxide layer can grow on either side of the existing oxide layer depending on whether the transportation mechanism is considered cation mobile or anion mobile as shown in Figure 15. As the oxide layer forms it slows the oxidation process by impeding the transportation of ions. Some types of oxides such as alumina (Al₂O₃) and chromia (Cr₂O₃) impede the transportation of ions enough that the oxide is considered a protective layer against further oxidation [70].

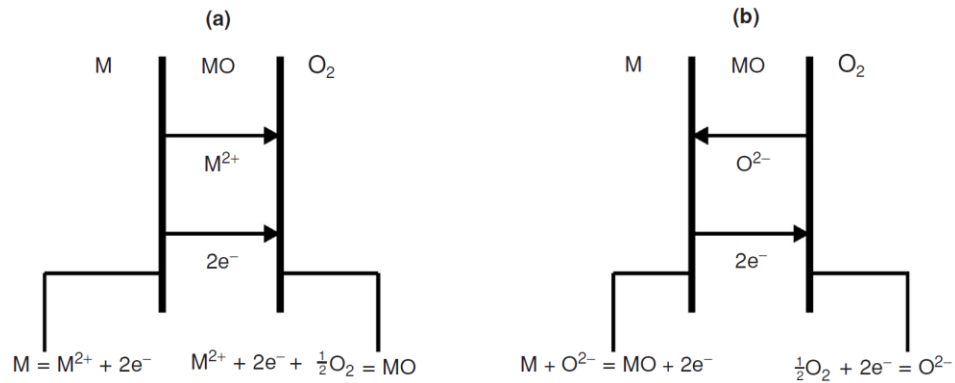


Figure 15: Transportation mechanisms and interface reactions of metal oxidation. a) cation mobile b) anion mobile [71].

2.6.2 Oxidation Rates

The rate of oxidation depends on several factors including the temperature, presence of oxygen, ion diffusion rates, alloy composition, and grain size. The diffusion rate of metal ions and oxygen ions through the oxide layer determines both the oxidation rate and at which interface the oxidation occurs. If the diffusion rate of metal ions through the oxide layer exceeds that of the oxygen ions, then the oxidation reaction occurs at the oxide-gas interface. Conversely, if the diffusion rate of oxygen ions through the oxide layer exceeds that of the metal ions, then the oxidation reaction occurs at the metal-oxide interface.

Temperature also plays a key role in determining the rate of oxidation for a given metal. The rate of oxidation is exponentially related to temperature, making it an Arrhenius relationship [72]. Similarly, for pure metals, it is known that the oxidation rate is proportional to the grain size [71]. Decreasing the grain size impedes the transportation of

metal ions such as Cr, Al, and Si to the metal-oxide interface and causes a decrease in oxidation rate.

Wagner's theory of oxidation presents a model for determining the oxidation rate of metals [69]. The theory explains ion transportation across an oxide layer using simplifying assumptions. In practice, the oxidation kinetics of different metals and alloys follow either a linear, parabolic, or logarithmic relationship [73]. Figure 16 shows the time dependent relationships of oxidation rate quantified by the total oxide mass.

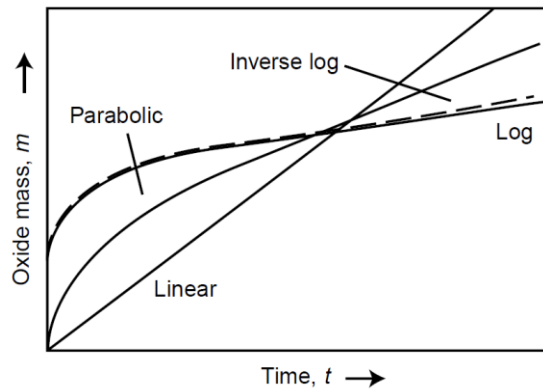


Figure 16: Different relationships for oxidation kinetics of metals [74].

In the case of a linear oxidation kinetic rate, the oxide scaled formed provides no protection to the base metal allowing the oxidation process to continue without resistance. Typically, this occurs in metals when the oxide undergoes cracking or spallation, when volatile oxides are formed, or when the oxide layer is very thin. The linear oxidation kinetic rate is expressed in Equation 2, where X is the oxide mass, k is the linear rate constant, and t is time.

$$X = kt \quad \text{Equation 2}$$

For metals exhibiting thick coherent oxides, such as Fe and Ni, the oxidation kinetic rate takes the form of a parabolic relationship where the reaction rate is controlled by ion diffusion through the oxide. The driving force of the ion diffusion is the chemical potential gradient across the oxide [73]. The oxidation rate is inversely proportional to oxide thickness as an increasing oxide thickness increases the ion diffusion distance. The parabolic oxidation kinetic rate is expressed in Equation 3, where k_1 and k_2 are relationship constants.

$$X^2 = k_1 t + k_2 \quad \text{Equation 3}$$

Typically, oxidation rate is determined either by measuring the thickness of the oxide layer or the increase in mass of the sample. Using the change in mass per unit area, the oxidation reaction can be represented by the Equation 4 and Equation 5, where V is the equivalent volume of oxide formed.

$$\left(\frac{\Delta m}{A}\right)_t^2 - \left(\frac{\Delta m}{A}\right)_{t_0}^2 = 2k''(t - t_0) \quad \text{Equation 4}$$

$$k'' = \left(\frac{8}{V}\right)^2 k' \quad \text{Equation 5}$$

The final oxidation kinetic rate takes the form of a logarithmic relation and typically occurs when an oxide layer forms at low temperatures. The driving force of the ion diffusion is the electric field across the oxide [73]. The logarithmic oxidation kinetic rate is expressed in Equation 6, where k and a are constants. In some cases, an inverse logarithmic relationship is also possible as shown in Figure 16.

$$X = k \log(at + 1) \quad \text{Equation 6}$$

2.6.3 Types of Oxidation in Nickel-Based Superalloys

Nickel-based superalloys generally form a chromia, Cr_2O_3 , or alumina, Al_2O_3 , oxide layer which protect from further oxidation. These oxides are what allow nickel-based superalloys to endure high temperature applications with minimal material loss due to spallation. For Ni-Cr alloys, including Hastelloy X, there are three different types of oxidation behaviors that can be encountered depending on the amount of Cr in the system.

Type I consists of alloys with less than 10% Cr content. In type I alloys, also known as dilute alloys, the rate constant k' is only slightly higher than that of pure nickel. The oxide scale in type I permits an increased diffusion rate of Ni ions due to doping of the scale with Cr.

Type II consists of alloys with between 10% and 30% Cr content. In these alloys, chromia forms primarily over external grain boundaries with some internal chromia formations present. Additionally, nickel oxide, NiO, forms externally over alloy grains.

Finally, type III consists of alloys with more than 30% Cr content. In these alloys the rate constant k' is several orders of magnitude lower than that of pure nickel.

For wrought Hastelloy X, research has shown that the oxides formed on the surface are composed of two layers; a manganese rich spinel as the outer layer and Cr_2O_3 as the inner layer [75].

Chapter 3: Experimental Procedure

This chapter details the experimental procedures used to conduct the research for this thesis.

3.1 Directed Energy Deposition Machine

All specimens created for this research were produced using a custom DED machine developed in-house at Carleton University. Since the machine uses wire feedstock material and an electric arc as the energy source it can be classified as a WAAM machine. The machine, shown in Figure 17, has a footprint of approximately 60 cm × 60 cm and stands nearly 90 cm tall. The build volume of the 3-axis machine is 300 mm × 300 mm × 300 mm. An onboard computer system controls stepper motors which drive ball screws to move the printhead along the horizontal plane in the X- and Y- directions and to move the build platform vertically in the Z-direction. The build platform includes a grid of threaded fastener holes allowing for rigid clamping of the substrate during material deposition. This was found to be essential for maintaining positional accuracy during the deposition process.

A Miller Diversion 180 TIG welder was used as the power source with a standard welding torch mounted to the print head. Local argon shielding is delivered through the torch, which is mounted such that the electrode is oriented vertically. The flow of current and shielding gas was controlled by the onboard computer system during deposition.

The wire feedstock delivery system uses a double drive wire feeder assembly originally intended for MIG welding. In its most recent configuration, the wire feeder assembly is

driven by a stepper motor and is mounted directly to the print head with the wire being fed at a fixed angle into the molten pool. The wire spool can either be mounted either directly to the side of the machine or under the table.

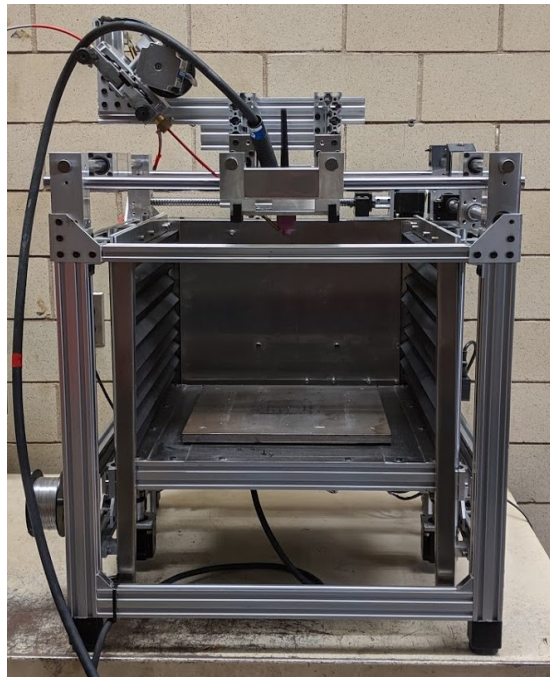


Figure 17: Wire-based directed energy deposition machine.

For this research work, 1.2 mm diameter welding wire was used and therefore the wire feeder assembly was configured with drive wheels for 1.2 mm diameter wire. Additionally, the torch was fitted with a 1.6 mm diameter 2% lanthanated tungsten electrode.

3.2 Material Selection

This research was conducted using Hastelloy X alloy (Haynes International) welding wire, a nickel-based superalloy. Properties and nominal composition of Hastelloy X are

discussed in Section 2.5.1. For the experiment, Hastelloy X was solution heat treated at 1177°C [2150°F] and cooled rapidly. Heat treatment was conducted on printed samples as well as sheet metal samples used as reference material. Hastelloy X was deposited onto consumable sheets of 304 stainless-steel substrate. 304 stainless-steel was selected as a suitable substrate material because of the low cost and weldability. All samples were deposited on 1/8" thick sheets. It is noted that in applications of WAAM, either the substrate can be considered a consumable material from which the part is removed after deposition or the process can be used to add features to an existing part therefore leaving the deposited material attached to the substrate. The substrate can be of similar or dissimilar composition to the AM material depending on the application.

3.3 Study of Effects of Process Parameters

In order to study the effect of process parameters on bead geometry and microstructure, first only a single bead was deposited on the substrate to reduce the number of variables in the problem.

As with many manufacturing processes, there are a significant number of factors that can affect the quality of the output. These factors include process parameters as well as environmental conditions that cannot easily be controlled. After careful consideration, the four most influential factors were selected for the experiment, wire feed rate, travel speed, current, and argon flow rate.

Each factor was given four levels, which are shown in Table 4. In order to consider all possible combinations, a full factorial experiment would require a total of 256 specimens. Therefore, to reduce the number of specimens in an efficient manner the Taguchi method was selected for this experiment. Design of experiments and the Taguchi method are described in Section 2.4.

Table 4: Experimental factors and levels.

	Level			
Factor	1	2	3	4
A: Wire Feed Rate (mm/min)	200	230	260	290
B: Travel Speed (mm/min)	84	96	108	120
C: Current (A)	50	53	56	59
D: Argon Flow Rate (CFH)	20	25	30	35

Since there are four four-level factors in this experiment, an $L_{16} (4^4)$ orthogonal array was selected which can be seen in Table 5. This effectively reduces the total number of specimens required to 16.

The specimens were evaluated using multiple criteria to observe the resulting trends and effects. The following evaluation criteria were used to characterize weld quality; bead roughness, bead width, bead height, melt through depth, and wetting angle. A bead with a low surface roughness possesses no major height variations or waviness which is considered beneficial when depositing multiple weld beads on top of each other to maintain a relatively constant working distance and geometric accuracy. The bead width, bead height, melt through depth, and wetting angle were measured to observe the effects of process parameters on the resulting geometry. The measurements were collected using ImageJ, an open source image processing software and are labeled in Figure 18.

Table 5: Experimental L_{16} (4^4) orthogonal array.

Sample #	Level			
	A Wire Feed Rate	B Travel Speed	C Current	D Argon Flow Rate
B01	1	1	1	1
B02	1	2	2	2
B03	1	3	3	3
B04	1	4	4	4
B05	2	1	2	3
B06	2	2	1	4
B07	2	3	4	1
B08	2	4	3	2
B09	3	1	3	4
B10	3	2	4	3
B11	3	3	1	2
B12	3	4	2	1
B13	4	1	4	2
B14	4	2	3	1
B15	4	3	2	4
B16	4	4	1	3

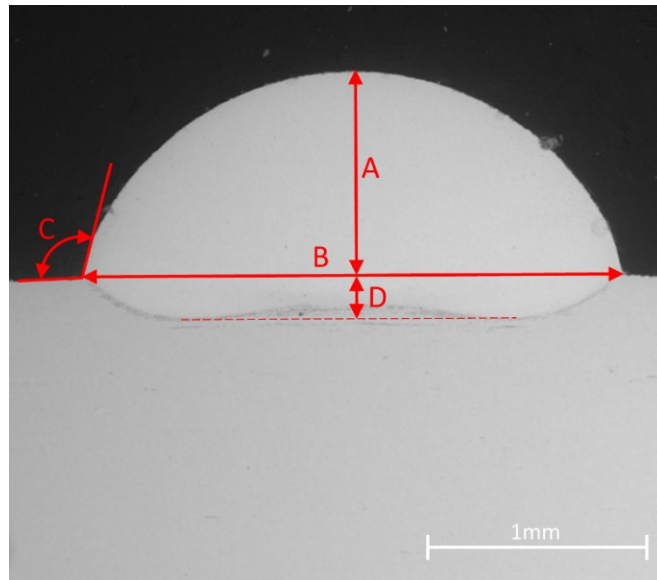


Figure 18: Sample geometry measurements in SEM A) height, B) width, C) wetting angle, and D) melt through depth.

The bead roughness was measured using a Veeco Dektak 150 Profilometer. An SEM was used to obtain qualitative and quantitative observations including the measurements labeled in Figure 18 as well as observing the microstructure, porosity, and secondary phase formation in the bead.

3.4 Sample Preparation

Prior to deposition, surface contaminants were removed from the 304 stainless-steel substrates by sandblasting with a Canablast ECONOBLAST sandblasting unit and cleaning with isopropyl alcohol.

For cross-sectional analysis after deposition, samples were cut free from the substrates using the Buehler Samplmet 2 abrasive cutter. The samples were then mounted in a phenolic resin puck using a Buehler Simplimet II before being grinding and polishing to the required surface finish.

For wear test and isothermal oxidation samples, the surface roughness on the vertical faces needed to be removed completely. The vertical faces were machined flat using several machining passes with an end mill, the progression of the process is shown in Figure 19. Once the faces were flattened, the printed material was removed from the substrate and cut to the required dimensions. Next, the specimens were annealed using a solution heat treatment at 1177°C [2150°F] for one hour and before being rapidly cooled in water. The heat-treated samples were then ground and polished to the desired surface finish. Specimens for isothermal oxidation testing were cut to approximately 10 mm × 10 mm and

the position within the printed structure was noted. Isothermal oxidation samples were ground to 1200 grit on all six faces. Wear test samples were cut to approximately 20 mm × 20 mm and mounted in a phenolic resin puck to fit the collar of the tribometer.

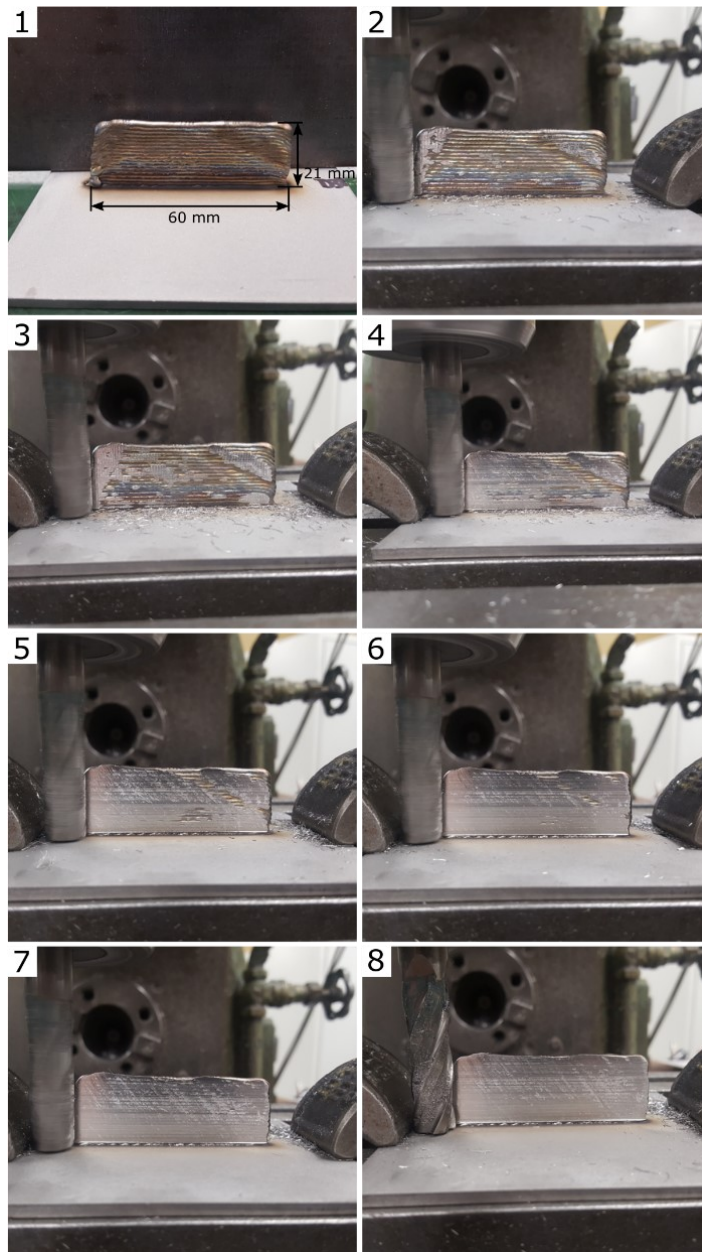


Figure 19: Progression of machining for sample preparation.

3.5 Isothermal Oxidation Testing

The specimens for isothermal oxidation testing were prepared per the methods described in Section 3.3. Additional details related to the results of the isothermal oxidation testing are included in Section 4.3. A 1000-hour isothermal oxidation test was completed with samples removed after 5 hours, 100 hours, 500 hours, and 1000 hours. Before beginning the test, all samples were cleaned thoroughly using an ultrasonic cleaner. In the ultrasonic cleaner, the specimens were each cleaned using a degreaser solution, acetone, and then water with each stage lasting 15 minutes. The specimens were removed from the final water bath and dried with a hot air gun.

Prior to beginning the test, all crucibles were degassed in a Carbolite STF 15/610 tube furnace at 1200°C [2192°F] to reduce the amount of potential weight change of the crucibles during the 1000-hour test. The dimensions of each specimen were measured and recorded to determine the surface area. The initial mass for each specimen and crucible, both individually and together, was measured three times and recorded.

When a specimen was removed from the furnace, it was cooled to room temperature before being placed on the balance. The mass of the combined specimen and crucible was recorded first in case of any spalling or material transfer from the specimen to the crucible. Then the specimen was removed from the crucible and each could be weighed separately. A standard sample was used to ensure proper calibration of the scale across the 1000 hour test period.

3.6 Hardness Testing

The hardness of printed specimens was measured using a Matasuzawa Co Hardness tester. Measurements were taken in Vickers hardness with a test force of 300 g. Hardness was measured in the additively manufactured specimens in the three directions shown in Figure 20. Measurements were taken at an even spacing across the length or height of the specimens.

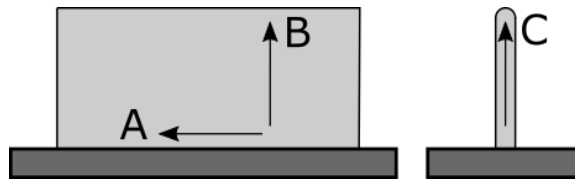


Figure 20: Position and direction of hardness measurements taken on additively manufactured specimens.

3.7 Wear Test

Wear testing was conducted using a pin-on-disk wear test setup. The machine used, shown in Figure 21, is a NEOPLUS NEO-TRIBO MPW110 Multi-Purpose Wear Test System. Additively manufactured and conventional wrought specimens were prepared and mounted in a phenolic resin puck as described in Section 3.4 . The machine was configured with a rotating pin set at a radius of 5 mm from the pin shaft axis. A new 5 mm diameter hardened 440C stainless steel ball bearing was used as the pin for each test. The ball bearings had nominal hardness of Rockwell C60. Wear loss was measured using the vertical displacement of the specimen collar relative to the pin shaft. A weight hanger was used to apply a vertical normal force between the specimen collar and the rotating pin. Tests were conducted under various sliding speeds, normal forces, and durations of time.

Testing proved to be problematic for both additively manufactured and conventional wrought specimens. The data recorded showed either a negative or negligible amount of wear loss. Sample test data is shown in Figure 22. It is suspected that this is due to material accumulation on the surface of the ball or within the wear track.

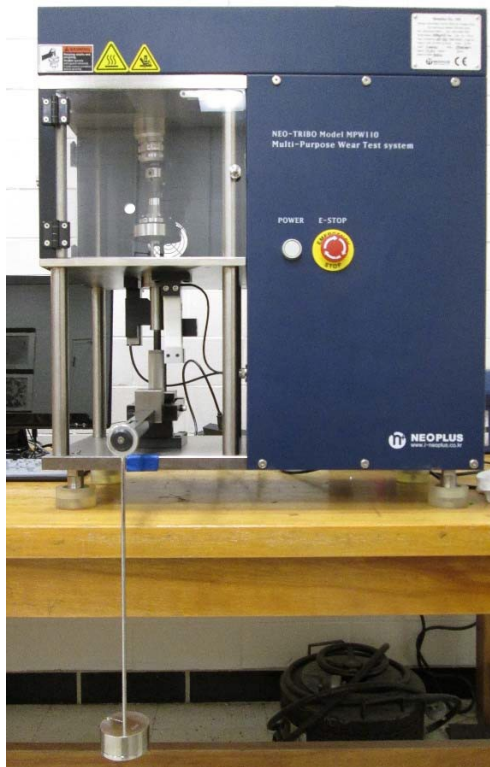


Figure 21: Pin-on-disk tribometer used for wear testing.

Additionally, after only several seconds of testing, an irregular chattering began to develop between the pin and the specimen. This caused the weight hanger to bounce during the test with the pin coming in and out of contact with the specimen. In some cases, the oscillations were considered too large and the test was stopped prematurely to avoid damaging the

equipment. Since the pin did not remain in contact with the disk and was repeatedly impacting the disk surface the results of testing were not considered to be reliable.

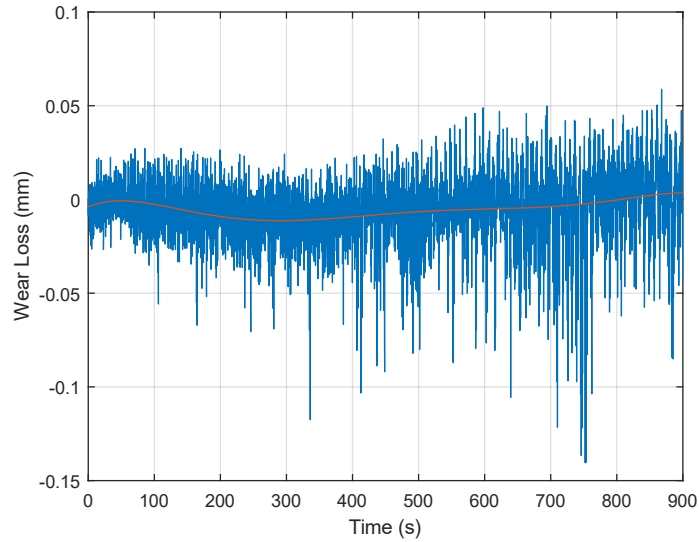


Figure 22: Sample wear test data.

Observations from optical microscopy indicated relatively deep and rough wear tracks formed on the samples. Additionally, the ball bearings were checked for wear or material build up. An image of both the specimen and ball bearing are shown in Figure 23.

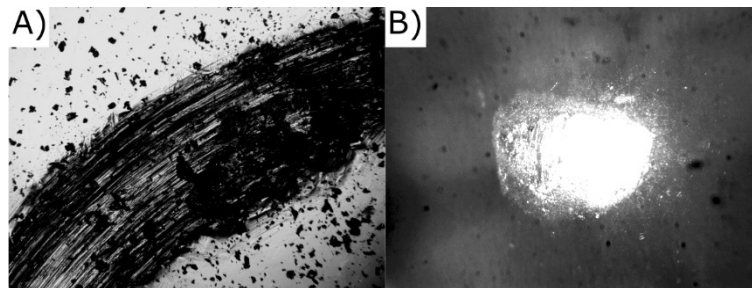


Figure 23: Sample wear track (A) and wear scar on ball bearing (B).

After each test, specimens were further analyzed using a profilometer to measure the depth and profile of the resultant wear track. Five separate measurements from the profilometer

were averaged to find the depth of the wear track as well as approximate the volumetric wear loss. A sample of these measurements is shown in Figure 24.

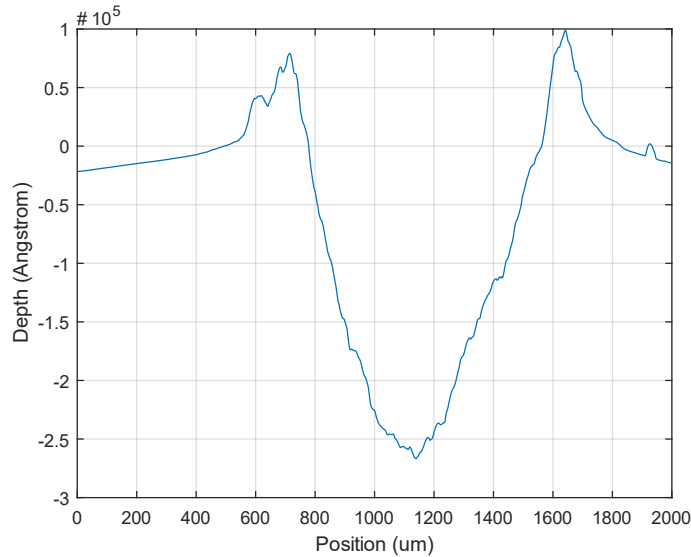


Figure 24: Averaged wear track profile.

3.8 SEM and EDS Analysis

A scanning electron microscope (SEM) was used to analyze the composition and microstructure of specimens. The specific SEM used was a Tescan Vega II XMU-SEM shown in Figure 25. The microscope is equipped with an Oxford X-ray detection system (INCA NES), a turbomolecular and rotary force vacuum pump, and four lenses capable of 10 nm resolution, a maximum magnification of 500 kx, and accelerating voltages from 0.2 kV to 30 kV.

Samples undergoing SEM analysis were prepared following the procedures discussed in Section 3.4. Once the samples were mounted, they were affixed onto a plate with conductive copper tape to ground the metal specimen to the SEM chamber.



Figure 25: Tescan Vega II XMU-SEM used for analysis.

Energy dispersive spectroscopy (EDS) was performed using the machine's x-ray detector to identify composition within the specimens. The specific phases were identified by comparing the EDS results to documented compositions using the Oxford INCA EDS software.

Chapter 4: Results and Discussion

Additive manufacturing of Hastelloy X was carried out using a TIG based WAAM system and the results are discussed in this section. First, the effects of print parameters on the resultant bead geometries and microstructures of single layer specimens is reported. Next, multilayer printing techniques are discussed with details regarding the different deposition strategies used. Finally, the isothermal oxidation behavior of Hastelloy X is compared between the additively manufactured specimens and the conventional wrought material.

The effect of varying process parameters of TIG based WAAM on specimen's geometry and microstructure were examined using Hastelloy X alloy (Haynes International) welding wire and 304 stainless-steel plate as the substrate.

4.1 Effects of Process Parameters

This section discusses the qualitative and quantitative examination of the effects of TIG process parameters on the attributes of the printed specimens. They were created according to the test matrix outlined in Section 3.3. All single layer specimens used for this analysis are shown in Figure 26 in a view perpendicular to the substrate surface. Figure 27 shows the beads at a low oblique angle to display the bead profiles.

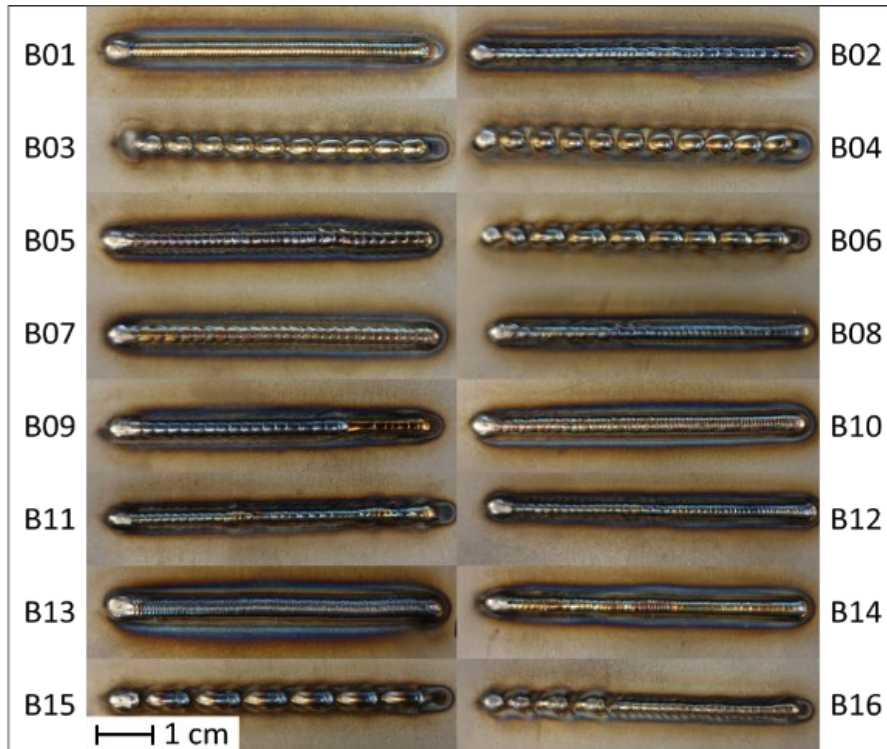


Figure 26: Top view of single layer weld beads.

Most of the specimens show signs of oxidation on the surface of the bead as well as in the heat affected zone of the substrate. The oxide layer formed mostly after the specimens were removed from the print bed and allowed to cool to room temperature through natural convection without the presence of shielding gas or any other form of oxidation protection. The oxidation appears as a blue or purple tint in most specimens (e.g. B05, B08, B13, etc.). As the oxide layer increases in thickness, the color transitions to a gold or straw color (e.g. B04, B07, B14, etc.).

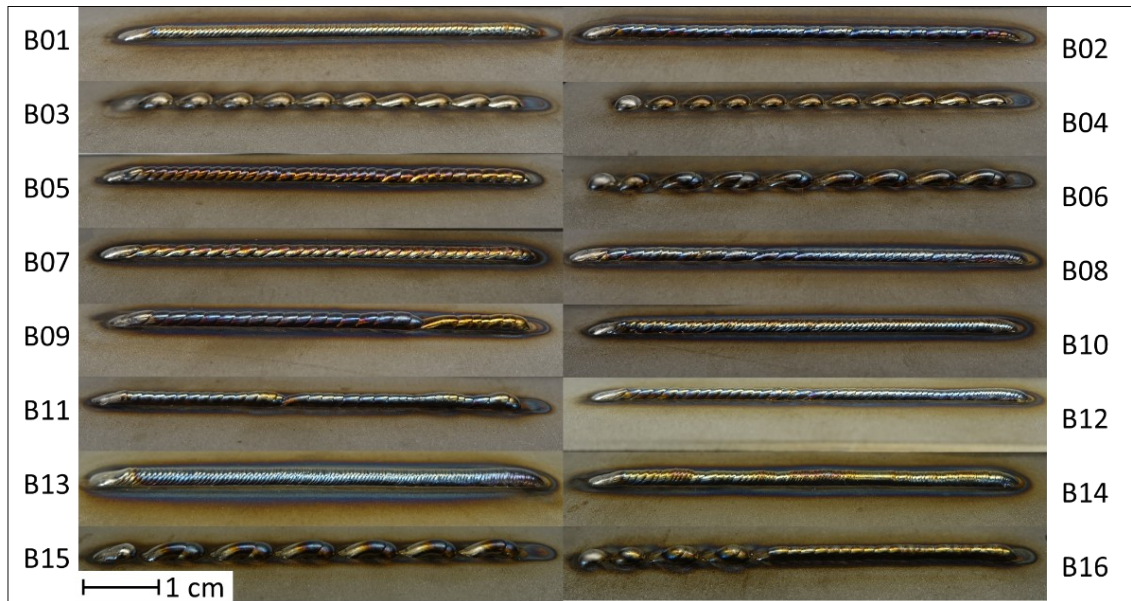


Figure 27: Low oblique angle view of single layer weld beads.

There are four specimens (B03, B04, B06, and B15) which formed arrays of discontinuous beads. In two of the cases, B03 and B04, the deposited droplets each remained separate whereas in specimens B06 and B15 the droplets are grouped in pairs. In all cases, the bead was not considered acceptable for AM applications due to their excessive height variations and discontinuities, therefore they were excluded from further evaluation.

The first evaluation criterion measured was bead roughness along the length of the bead. Profilometer data provided an arithmetic average roughness of the weld bead. Two measurements were made at different locations on each specimen which were averaged to produce a final value for evaluation purposes. A lower roughness value was considered desirable since there would be less variation in working distance during the deposition of

subsequent layers. The highest average roughness recorded was 62.8 μm and the lowest average roughness was 16.8 μm .

Using the SEM, the microstructure of the bead, the substrate, and the bead-substrate interface were observed as shown in Figure 28.

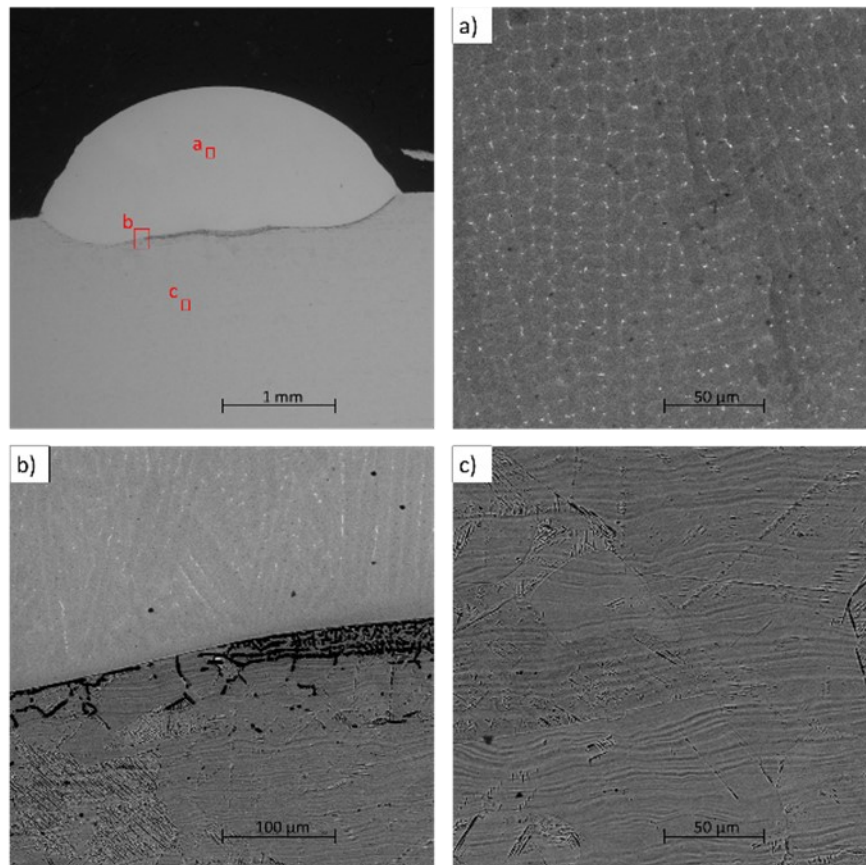


Figure 28: SEM images showing bead and substrate microstructure (Sample B10).

Figure 28 a) and b) show the columnar grain structure in the bead, nucleating from the bead-substrate interface (i.e., epitaxial growth [76]) and transitioning to a cellular grain

arrangement higher in the bead. The columnar structure occurs since the substrate is not preheated and therefore a large temperature gradient is present at the bead-substrate interface. Towards the top of the bead, the grains begin to form in a cellular arrangement as the temperature gradient is reduced and heat is transferred from the molten pool at a slower rate.

In Figure 28, it is noted that within the interface the center is raised slightly whereas the two edges penetrated deeper into the surface of the substrate. These geometrical features are referred to as ‘humping’ and ‘undercutting’. ‘Humping’ and ‘undercutting’ can be caused by the fluid flow within the molten weld pool [77]. The suspected driving force behind the flow is that of the Marangoni effect, or more specifically the thermocapillary effect, where variations in surface tension cause the fluid flow [78].

The weld pool fluid flow may also be used to explain the presence of defects at the bead to substrate interface which can be seen more clearly in Figure 29. The fluid flow in the bead circulated radially inwards at the top causing a downward flow at the center of the bead to form. The interfacial defects were concentrated near the center of the bead suggesting that this flow may have swept gases towards the center of the bead during the solidification process.

For the purposes of AM, the substrate is often considered a consumable material which is removed. In cases where the substrate is part of the final part (such as in the application

where details are created on a metal die using AM technology) efforts must be made to reduce the presence of these voids at the interface.

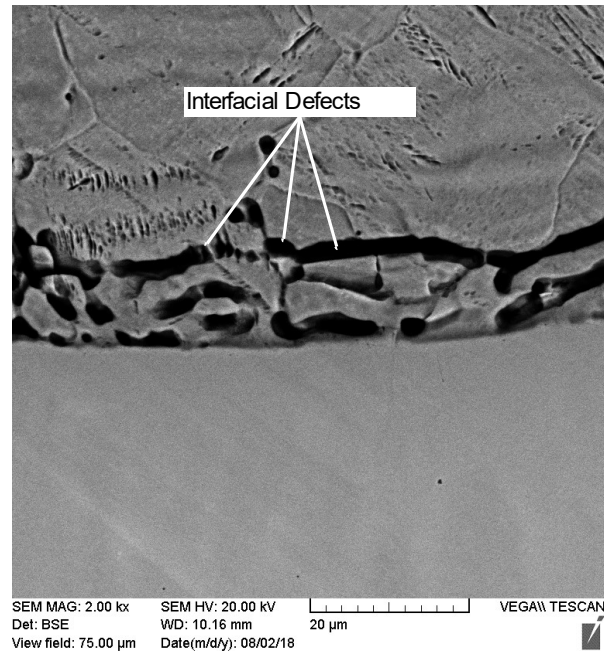


Figure 29: Voids at the bead-substrate interface (Bead shown on top).

Energy-dispersive X-ray spectroscopy (EDS) analysis was performed to analyze the compositional change across the diffusion zone between the substrate and the bead. A color map is shown in Figure 30, illustrating the concentration of several elements across the interface. Additionally, a quantitative line scan was performed, yielding the graphs shown in Figure 31 and Figure 32. The interface can be clearly identified in the graphs of elements such as iron, nickel, and molybdenum.

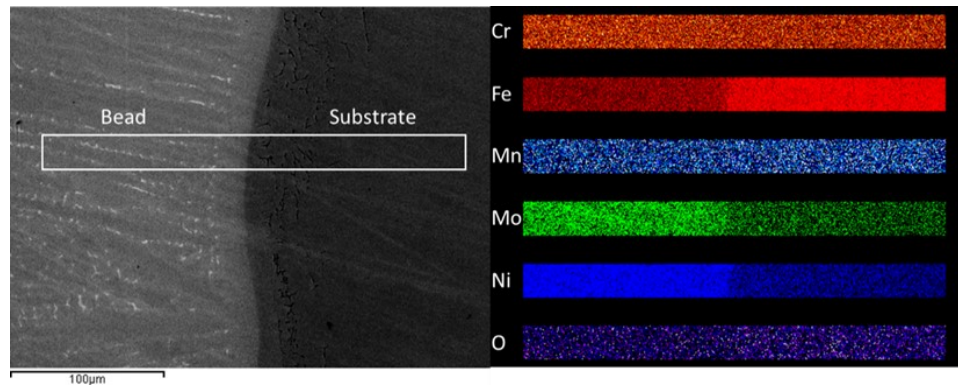


Figure 30: Elemental scan results across bead-substrate interface (Bead shown on left).

Finally, EDS was also used to identify the presence of carbides in the bead. By comparing the relative composition of carbon and molybdenum in the precipitates to that of the matrix the presence of molybdenum carbides can be confirmed. The carbides take the form of intragranular precipitates as labeled in Figure 33.

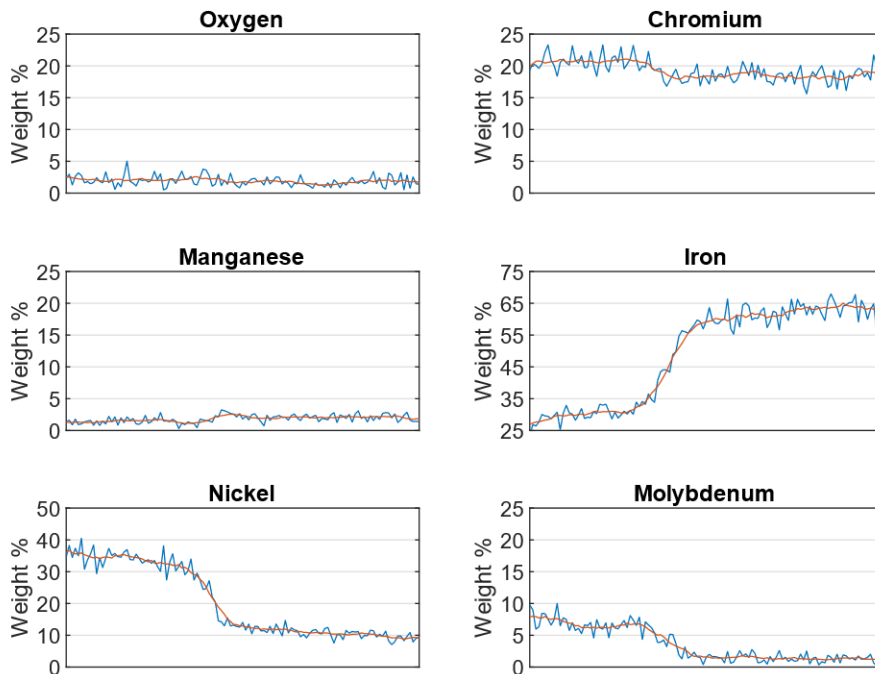


Figure 31: Quantitative EDS analysis across bead-substrate interface (oriented in same direction as labeled in Figure 30).

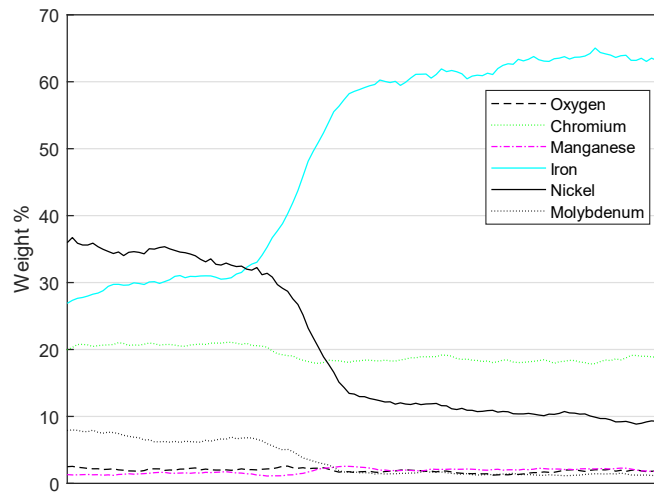


Figure 32: Composite plot of EDS scans (10 point moving averages) across bead-substrate interface (oriented in same direction as labeled in Figure 30).

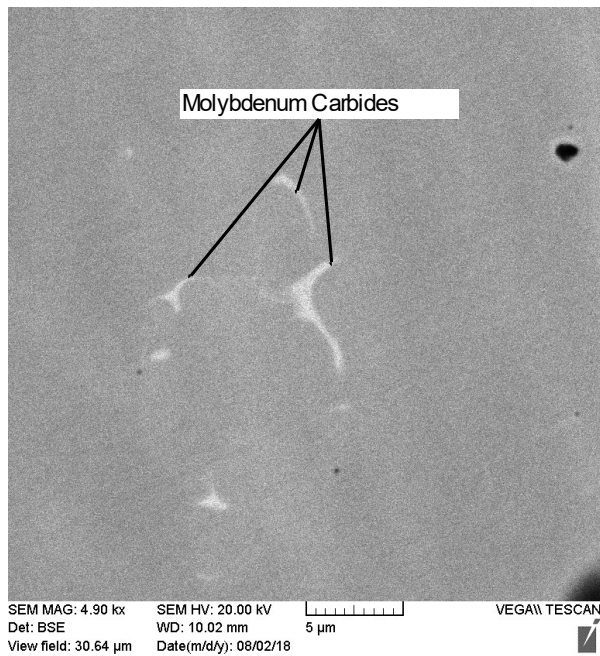


Figure 33: Molybdenum carbides present in bead material.

The size and distribution of the carbide precipitates significantly change material properties such as strength and ductility [79]. Therefore, it is key to control their size and distribution throughout an additively manufactured part. The size and distribution of molybdenum carbides is discussed further in Section 4.2 where the carbides are monitored throughout the thicknesses of multi-layered specimens.

4.1.1 Analysis of Variance (ANOVA)

Statistical analysis was performed using Minitab 18 and selected interval plots are shown in Figure 34 and Figure 35. The first factor observed is the wire feed rate. The bead height increases in an approximately linear fashion as the wire feed rate increases and the bead width decreases only at the second feed rate. Since a higher wire feed rate results in a taller and narrower bead, the aspect ratio increases while the wetting angle decreases. Both the melt through depth and the roughness are considered independent of the wire feed rate.

The travel speed is considered next and in this case the bead width is shown to decrease with travel speed whereas the bead height does not vary significantly. This of course means that wetting angle decreases with travel speed. Unlike wire feed rate, the travel speed significantly impacts the melt through depth, which decreases as the travel speed increases.

Since the travel speed is increasing the heat input decreases and therefore the melt through depth is also expected to decrease. The bead roughness also shows a slight increase as the travel speed increases.

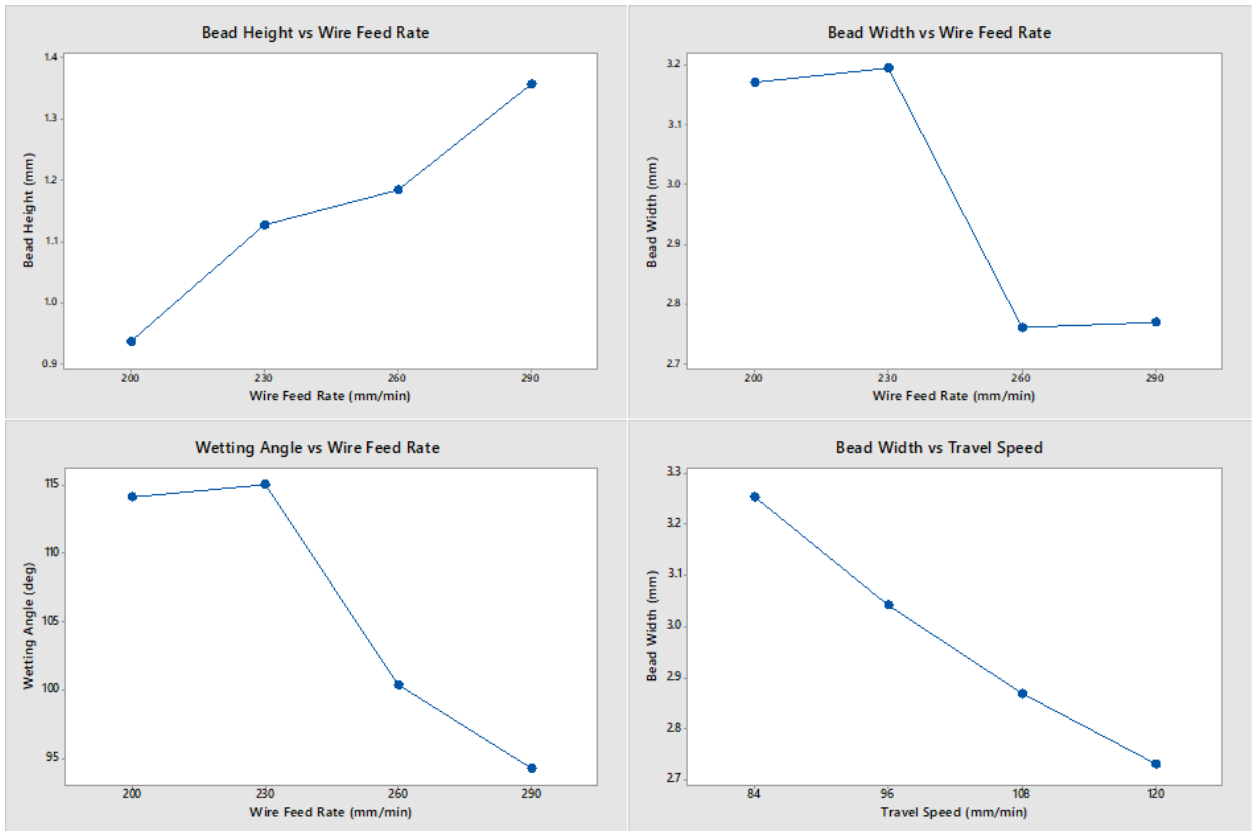


Figure 34: Interval plots displaying significant trends between factors and responses.

Since current and travel speed have an inverse effect on heat input, many of the trends are similar except with an inverse direction. Current shows the most significant impact on the bead roughness, with a small peak at the second level and then decreasing as current increases. The bead width is shown to increase with current and the bead height does not vary significantly. This results in an increase in wetting angle with current. Finally, the melt-through depth increases with an increase in current since the heat input is increased when other parameters are kept constant.

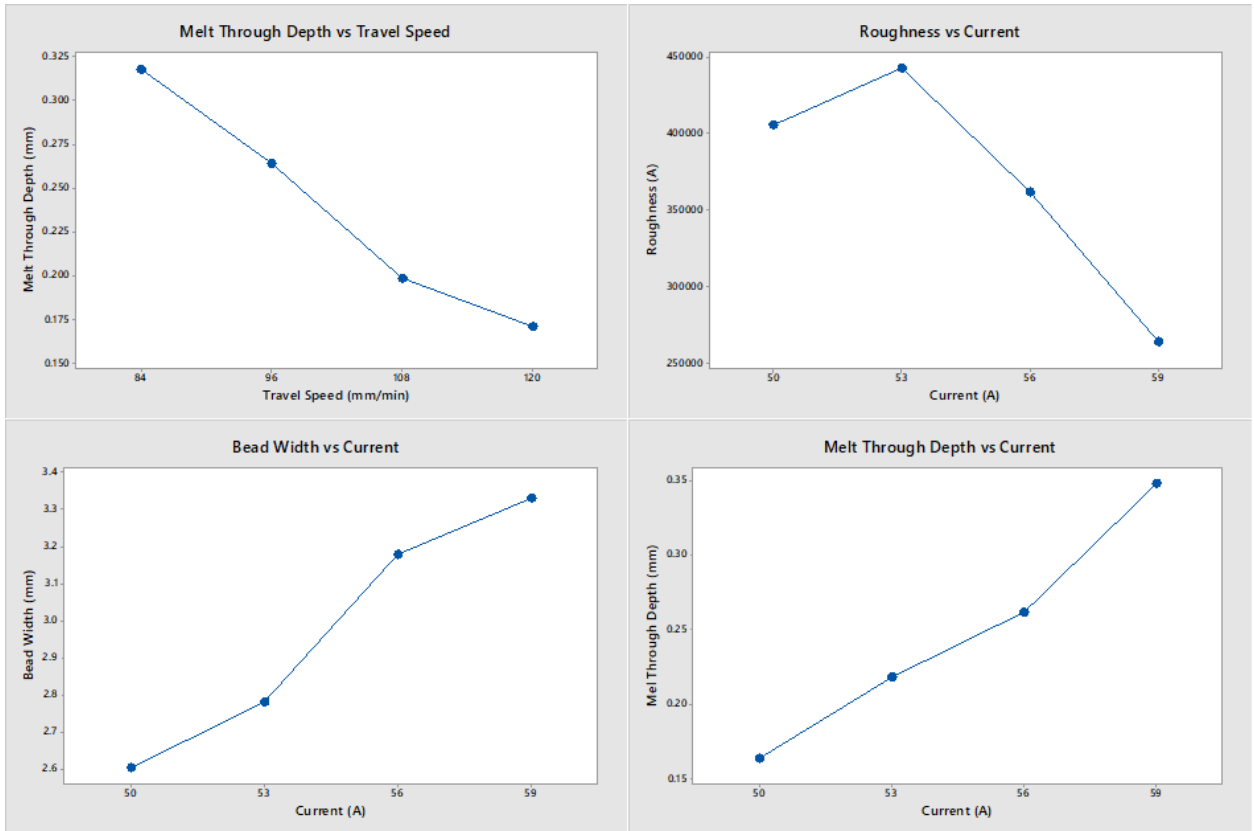


Figure 35: Interval plots displaying significant trends between factors and responses.

The argon flow rate was also considered during the ANOVA, however, it resulted in no significant effects on the bead height, bead width, wetting angle, melt through depth, or roughness. This suggests that in future work, the argon flow rate does not need to be considered as a critical input variable and can be maintained at a constant level determined by the extent of oxidation.

4.2 Multi-layered Samples

Results of various deposition strategies are discussed in this section. Preliminary trials were first performed to develop an understanding before the process was refined to improve the

quality of printed samples in terms of dimensional consistency and lack of oxidation or defects.

4.2.1 Preliminary Trials

Preliminary trials were performed using the printing parameters of Sample B10 for the first layer since it yielded excellent results in all measured responses with repeatable results.

Deposition strategies were first tested by creating three-layer specimens where each specimen employs different deposition strategies, as shown in Figure 36. Specimens were created either with consecutive layers deposited in the same direction or alternating directions and with a heat input reduction of either 5% or 20% between each consecutive layer.

First, the difference between printing consecutive layers in the same direction versus alternating directions was explored. It was believed that depositing all layers in the same direction could result in a greater height at the end of the weld path and a lower height at the beginning potentially caused by a lag in the wire feed system which would be compounded by each subsequent layer. Alternating print directions between layers was expected to reduce this effect. However, the specimens shown in Figure 36 demonstrate that repeating the same print direction or alternating the print direction produces no significant difference in the bead shape for a three-layer specimen. This may not hold true for specimens with more layers as any small difference in height at the beginning or end of the bead will be magnified by each subsequent layer.

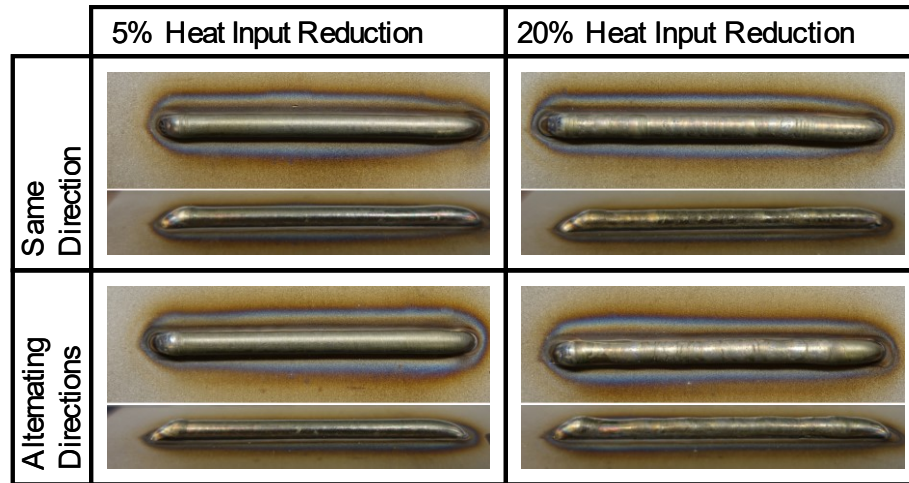


Figure 36: Three layered specimens used to compare printing strategies. Each specimen shown in two views: top view (top) and low oblique angle view (bottom).

For these initial specimens, no interpass pause time (hence cooling) was used. Instead, the heat input was reduced sequentially between each layer. Based on the findings of some preliminary trials, the heat input was decreased by either 5% or 20% between each layer. The decrease in heat input was in fact achieved by increasing the travel speed of each pass while maintaining a constant current. As seen in Figure 36, no significant difference in bead shape, surface quality, or oxidation level can be observed between the samples with 5% reduction and 20% reduction of heat input. However, in samples with 5% reduction it was observed from the on-board camera that during the third pass the two previous layers were completely remelted, indicating an excessive amount of heat input. Therefore, for further specimens it was decided to continue with a 20% decrease in heat input between each consecutive layer. This value will vary significantly based on the size and shape of

the part to be printed and therefore to optimize this value a thermodynamic study of the process would be required.

Contrary to the single layer specimens, the oxidation on the surface of the bead changed from a colorful blue or gold tint to a dull grey. This suggests a thicker oxide layer formed on the surface of the bead. Similarly, the oxide layer was observed mostly after the specimens were removed from the print bed and allowed to cool through natural convection at room temperature. The thick oxide layer was likely as a result of both excessive heat input and lack of shielding gas during cooling.

Three additional samples (B41, B42, and B43) were created based on the findings of these preliminary trials. Their respective printing parameters are summarized in Table 6. Samples B41 and B42 are made of four layers, each with alternating print directions and a 20% decrease in heat input between subsequent layers. It was noted that these printing parameters yielded excellent repeatability with almost no visible differences between samples B41 and B42.

Sample B43 was created with a total of eight layers using alternating print directions and a 20% decrease in heat input between layers for the first four layers, after which a steady state was believed to have been reached, and the heat input was subsequently held constant. The steady state zone was determined through trial and error testing where it was noted that further reduction in heat input resulted in extremely poor surface roughness or

incomplete melting of the wire. All three samples can be seen in Figure 37 with their respective cross sections.

Table 6: Process parameters used for multi-layer samples (B41, B42, and B43)

Layer	Travel Speed (mm/min)	Wire Feed Rate (mm/min)	Current (A)	Argon Flow Rate (CFH)
1	96	260	59	30
2	115.2			
3	138.2			
4	165.9			
5 (B43 Only)	165.9			
6 (B43 Only)	165.9			
7 (B43 Only)	165.9			
8 (B43 Only)	165.9			

As shown in Figure 37, samples B41 and B42 have a very smooth bead profile with no variation in height at the beginning nor the end of the bead. Sample B43 however has a rougher and more irregular surface and a large buildup of material is present at both ends of the sample. This buildup is believed to be caused by a slight pause while the torch is raised between layers. During this vertical motion the arc is not terminated and therefore the wire continues to melt and is deposited at the end of the bead. This effect is compounded by each subsequent layer which explains its absence in the four-layer specimens. To prevent this from occurring in future work, either an interpass pause was used or the computer control was set to temporarily stop the arc or reduce the current while raising the torch for deposition of subsequent layers.

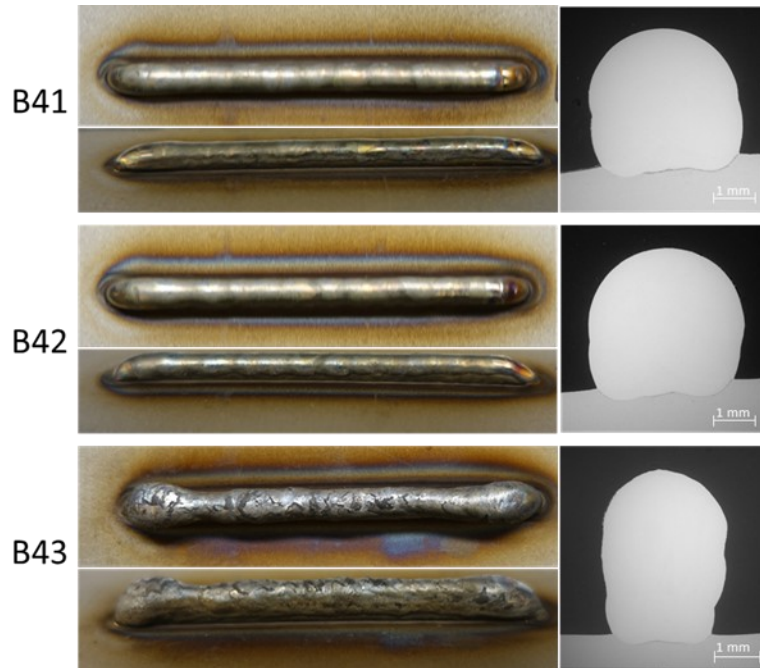


Figure 37: Multiple layer specimens shown in two views with cross sections on the right.

The microstructure of the cross sections of specimens B41, B42, and B43 does not reveal any observable interface between the layers (Figure 37 and Figure 38). This suggests a complete fusion between layers with no oxidation present. Since no interpass pause time was used, the argon shielding gas continued to flow between layers and effectively protected from oxidation. When an interpass pause time is used it is important to maintain the argon flow for oxidation prevention.

The size and shape of the molybdenum carbides in microstructure vary significantly between layers suggesting that there is a significant difference in thermal history between layers (Figure 38). Three distinct zones are observed in the figure. First, nearest to the bead-substrate interface, the carbides are finer and evenly distributed amongst the columnar

grain matrix. This first zone is shown in Figure 38 a). The small and evenly distributed carbide formations are caused by the large temperature difference between the cold substrate and the molten wire material. The larger thermal gradient leads to increased directional carbide initiation and reduced time for carbide growth. The second zone is seen in Figure 38 b), c), and d) where the carbides grow larger and reduce in number. This is due to subsequent reheating when the next layer of material is deposited, resulting in a relatively slow cooling rate for carbide nucleation. The third and final zone is seen at the top of the bead (Figure 38 e). The carbides return to a fine and even distribution due to the reduced heat input at this stage except now distributed in a cellular form. In the third zone, the molten metal is cooled quickly through convection and is not remelted since no subsequent layers are added.

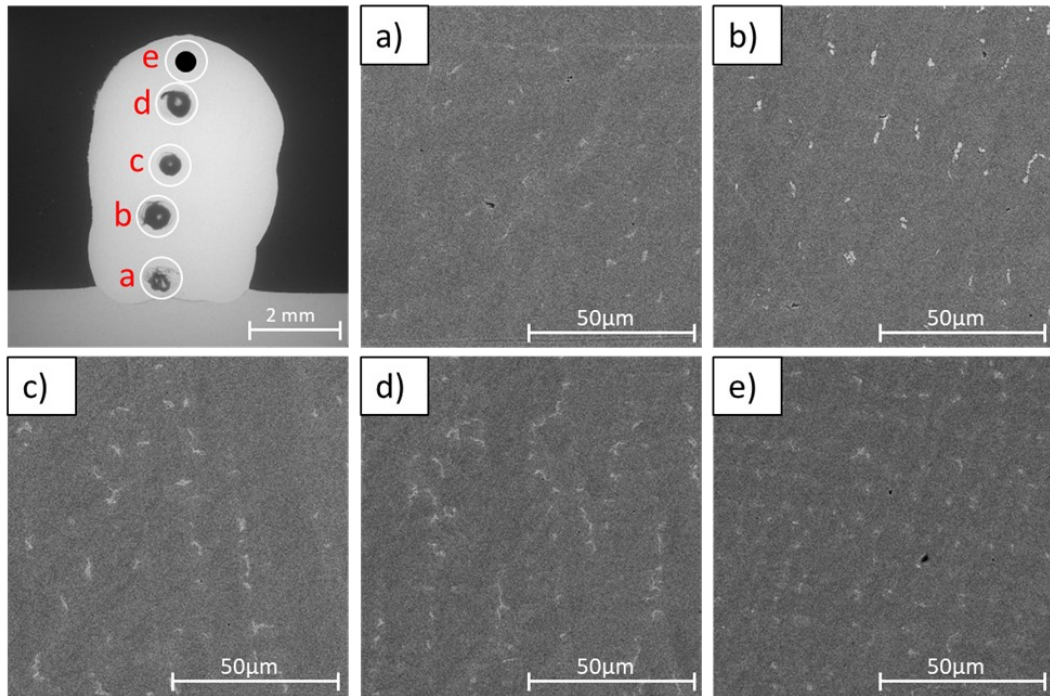


Figure 38: Microstructure of specimen B43 from bottom to top of cross section.

Inconsistent carbide distribution will cause material properties to vary within the part. Depending on the application and the desired material strength, ductility, and hardness, post additive manufacture heat treatment is usually carried out. The printing strategies presented in this section results in non-uniformly distributed carbides throughout the specimen. To improve the microstructure, the heat input may be reduced by increasing welding speed in order to avoid excessive carbide growth or a post additive manufacturing heat treatment may be used to redistribute the carbides and homogenize the microstructure.

4.2.2 Final Results of Multi-Layer Samples

With an understanding of process behavior in multi-layer samples, the deposition process was refined to improve specimen quality. Specimens were created with each layer deposited in the same direction. The heat input was gradually decreased between each layer for the first five layers, after which a steady state was believed to have been reached, and the heat input was subsequently held constant. Process parameters used to create all multi-layered samples used in this section, for surface analysis, wear testing, and isothermal oxidation are shown in Table 7.

Table 7: Final process parameters used for multi-layer samples

Layer	Current (A)	Travel Speed (mm/min)	Wire Feed Rate (mm/min)	Argon Flow Rate (CFH)
1	60	100	350	25
2	48			
3	40.8			
4	35.4			
5	31.2			
6 +	31.2			

Compared to previous multi-layered samples, these new samples were of significantly higher geometric uniformity with reduced discoloration and could be manufactured with 20 or more layers reaching wall heights in excess of 2 cm. Figure 39 shows one of these samples immediately after printing. Similar to the single layer samples, the surface oxidation is presented in the form of a purple, blue, and gold tint. This suggests that the oxide layer has been significantly reduced compared to previous multi-layered samples where the oxides were a dull grey color. This is likely due to the reduced heat input, and continued flow of shielding gasses during the short pause between layers.

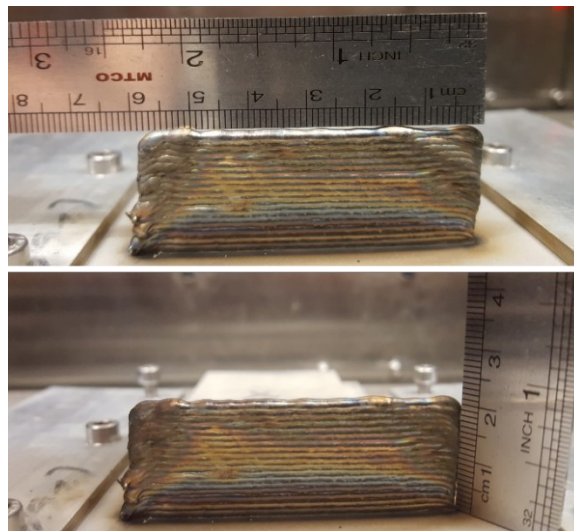


Figure 39: Sample of typical multi-layered specimen.

It is noted that there is no significant variation in height at the beginning or end of the passes. Small variations in layer height however are carried through between layers as can be seen in Figure 39. A cross section of the specimens reveals visual distinctions between layers which can be seen in Figure 40, including both optical and SEM imaging of the microstructure at various location along the height of the specimen.

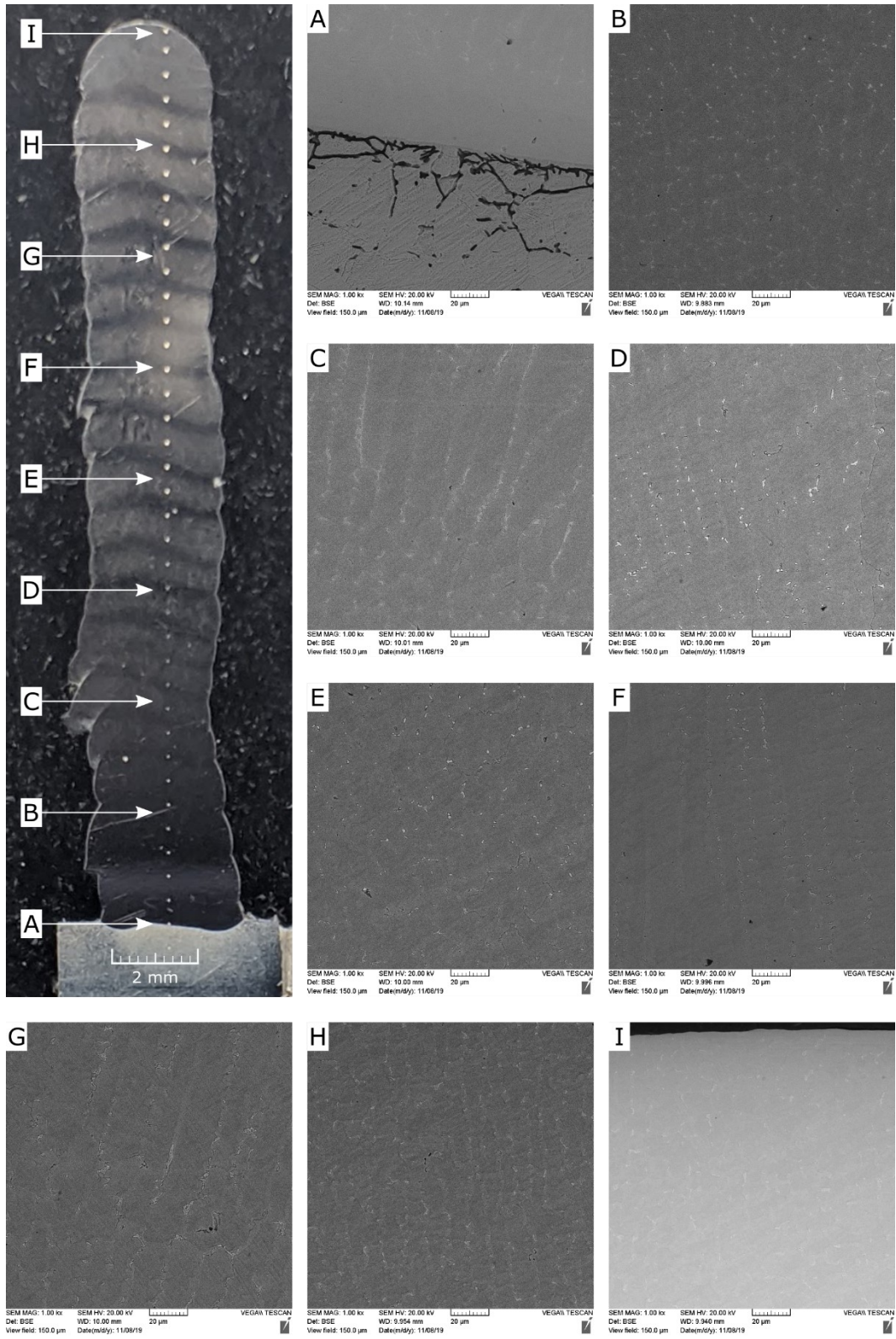


Figure 40: Cross sectional microscopy of AM sample.

Compared to previous specimens, the layers are better delineated through the entire height of the specimen. Microscopy confirms that a complete fusion is achieved between layers. The distinct boundaries are likely due to the implementation of a short interpass pause time which allowed the previous layer to cool more than in previous samples. Additionally, there may have been some oxides formed during the pauses since the shielding gas may not completely exclude oxygen. A fully enclosed inert environment would be required to completely remove the chance of oxide formation between layers.

The size and shape of the molybdenum carbides in microstructure varied less significantly between layers suggesting that the heat input was reduced sufficiently such that the previous layers were not remelted during subsequent deposition. The carbides are relatively fine and evenly distributed across the height of the specimen as seen in Figure 40. Most of the grain structure exhibits a cellular arrangement with some columnar grain structures formed near the base and tip of the specimen due to slightly higher temperature gradient.

Further analysis was conducted to determine the mechanical properties of the microstructure. Hardness testing was conducted in three separate directions as shown in Figure 41. In all three test directions, the hardness measurements were taken at an even spacing of 560 μm . All three test directions show little to no variation in hardness along the length of the test, suggesting that the thermal history within the specimen was either relatively constant throughout or does not significantly impact the hardness of the specimen.

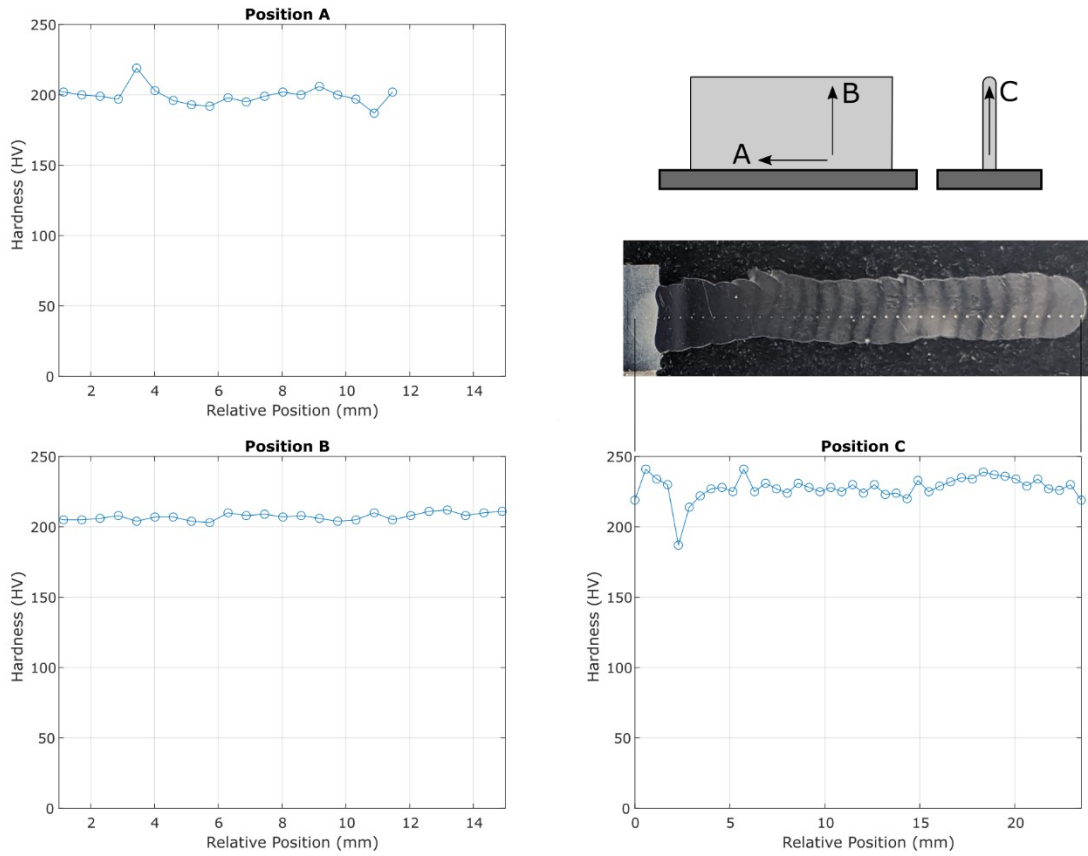


Figure 41: Hardness testing along build direction of AM specimen.

4.3 Isothermal Oxidation Testing

Hastelloy X samples were subjected to isothermal oxidation in air at 1080°C for up to 1000 hours. The testing temperature was selected based on typical creep temperatures and high temperature tensile properties of Hastelloy X. Samples were removed from the furnace after 5 hours, 100 hours, 500 hours, and 1000 hours to determine the weight gain per surface area. The results, plotted in Figure 42, are in the form of $(\text{mass change}/\text{surface area})^2$ vs time. Oxidation of a wrought sheet sample of Hastelloy X was also measured for

500 hours as a baseline and the results are also plotted in Figure 42. The trend line included in Figure 42 indicates that the parabolic rate law of oxidation is obeyed.

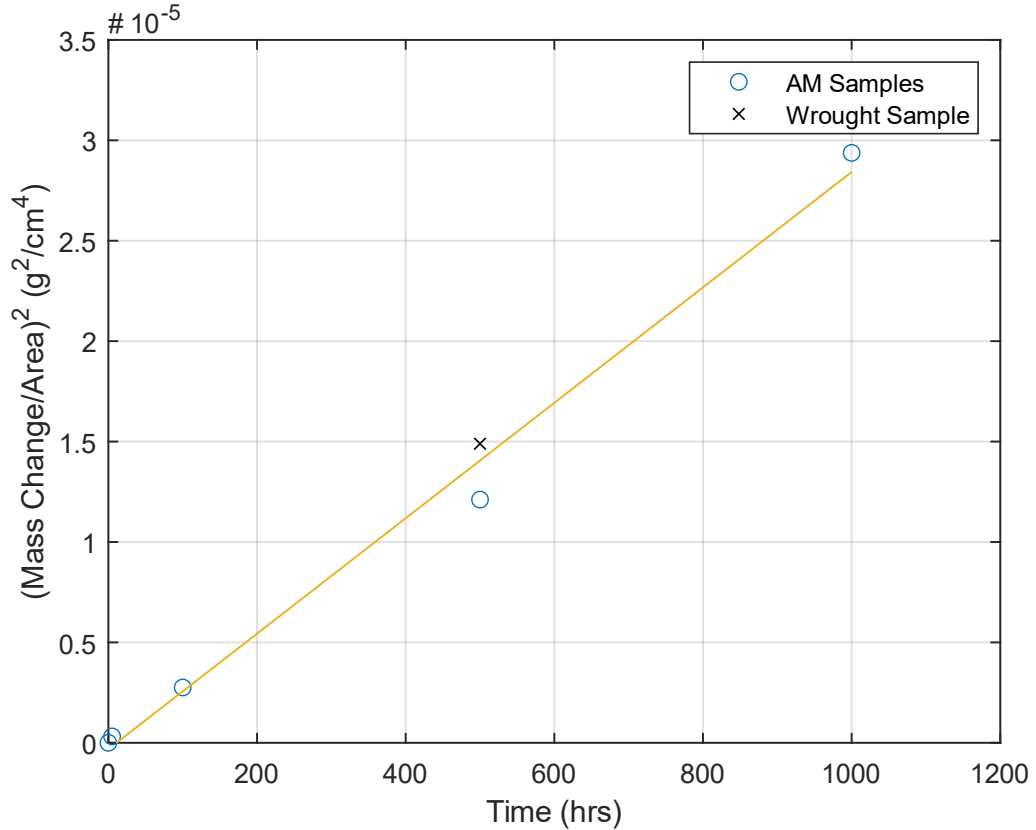


Figure 42: (Mass change/area)² vs time for isothermal oxidation of Hastelloy X at 1080°C.

From the linear regression model, the parabolic oxidation rate constant, k_1 , for the printed samples was found to be $4.54 \times 10^{-8} \text{ g}^2/\text{cm}^4/\text{h}$. In published literature, the parabolic rate constant for the oxidation of Hastelloy X in air was found to be $4.58 \times 10^{-8} \text{ g}^2/\text{cm}^4/\text{h}$ at 1050°C and $1.20 \times 10^{-7} \text{ g}^2/\text{cm}^4/\text{h}$ at 1100°C [80]. The published values for parabolic oxidation rate constant are higher than the experimental value obtained in this study,

indicating that the AM samples may have an advantage in oxidation resistance due to finer grains and perhaps a better composition uniformity [81].

The wrought sample oxidized for 500 hours experienced more weight gain than the AM sample at the same duration revealing that more oxide was formed on the wrought sample. However, the wrought sample matches closely with the linear regression fit to the AM samples suggesting that the oxidation behavior of both materials is similar.

Using SEM images, the oxide scale thickness was recorded for each sample after oxidation. For each specimen, the oxide thickness was measured five times in three different locations in order to account for variations in thickness. Sample images from this process are shown in Figure 43. After only 5 hours in the furnace, a very thin oxide layer is already present. The oxide forms in a very smooth and even layer on the surface of the specimens. As the oxide layer grows in thickness with time the exposed surface becomes uneven. Additionally, the metal-oxide interface becomes less easily defined with each time interval due to different oxide growth rates.

The quantitative results, plotted in Figure 44, are in the form of oxide thickness versus time. At the beginning of the experiment, it is seen that the oxide thickness grows rapidly, as it has been seen on other materials during the transient state when protective surface oxides have not been established. Over time, the oxidation rate slows significantly and appears to reach an asymptotic limit. The oxidation rate is expected to decrease over time as the adherent oxide impedes the diffusion of chromium ions [70], [81]. The wrought

sample is shown to have formed a slightly thicker oxide layer than the AM samples. However, like the mass change findings mentioned previously, the difference is not significant enough to state an increased oxidation resistance of the AM samples.

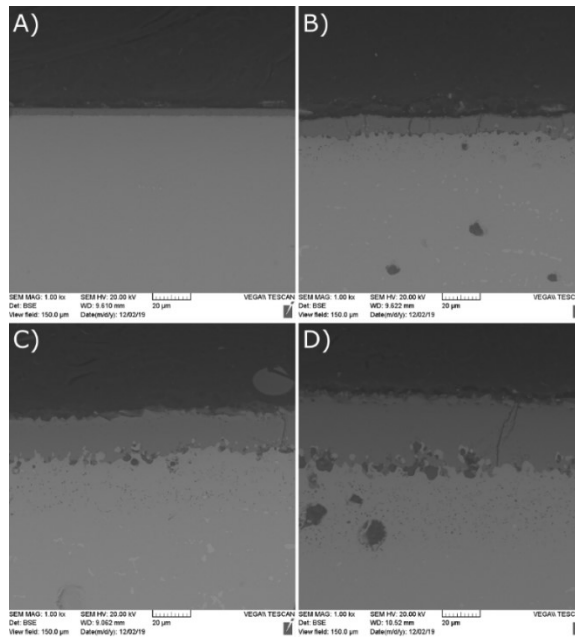


Figure 43: SEM imaging of surface oxide thickness after A) 5 hours, B) 100 hours, C) 500 hours, and D) 1000 hours.

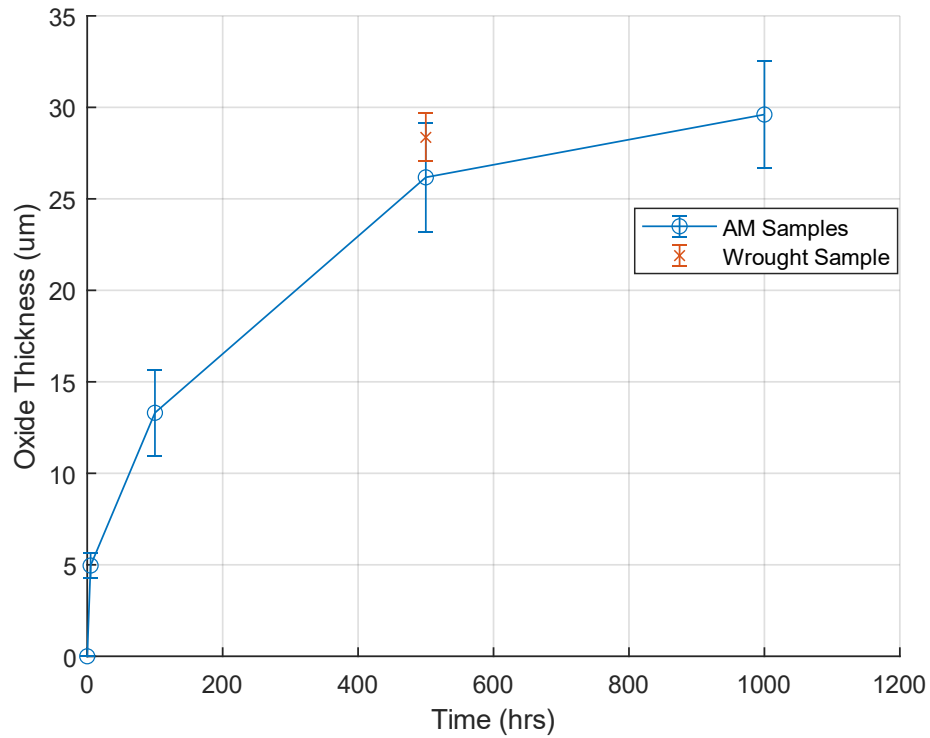


Figure 44: Oxide thickness vs time for isothermal oxidation of Hastelloy X at 1080°C.

Some spallation was observed in the 1000-hour samples as shown in Figure 45. The spallation was considered relatively minor and ejected material was contained within the crucibles. Prior to removing the specimens from the crucibles, the mass of the crucible and specimens together was recorded to find any discrepancy in mass gain.

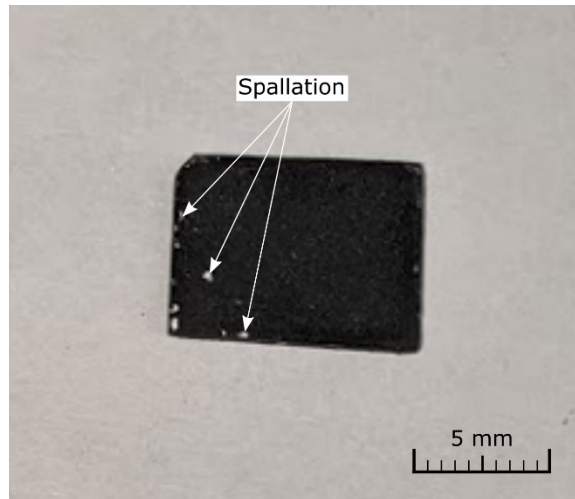


Figure 45: Example of spallation present on 1000-hour specimens.

Energy-dispersive X-ray spectroscopy (EDS) analysis was performed to analyze the composition of the oxide layer as well as the compositional change near the exposed surface. The analysis was performed on both an AM sample and a wrought sample after 500 hours of oxidation in the furnace and the results are shown in Figure 46 and Figure 47 respectively.

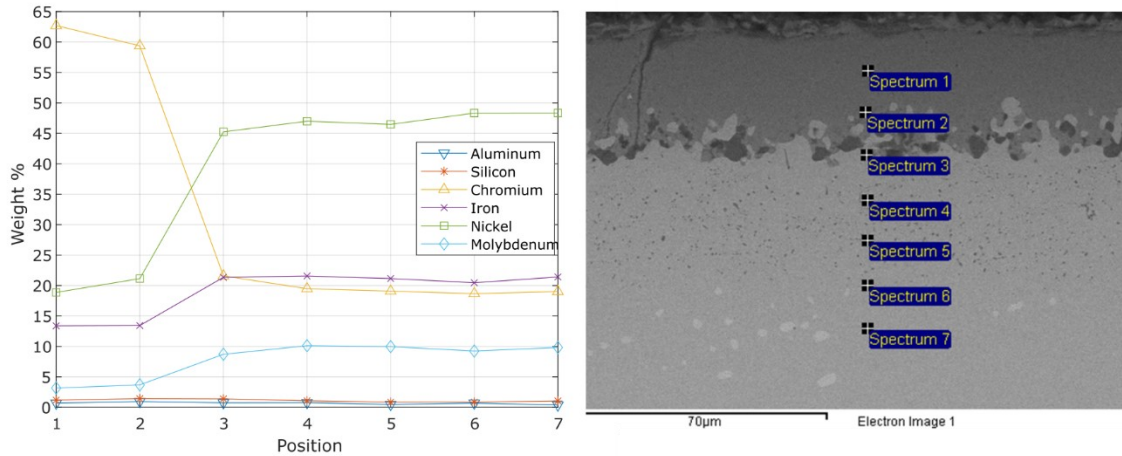


Figure 46: Quantitative EDS analysis across the oxide-substrate interface of an AM sample after 500 hours (oxygen omitted).

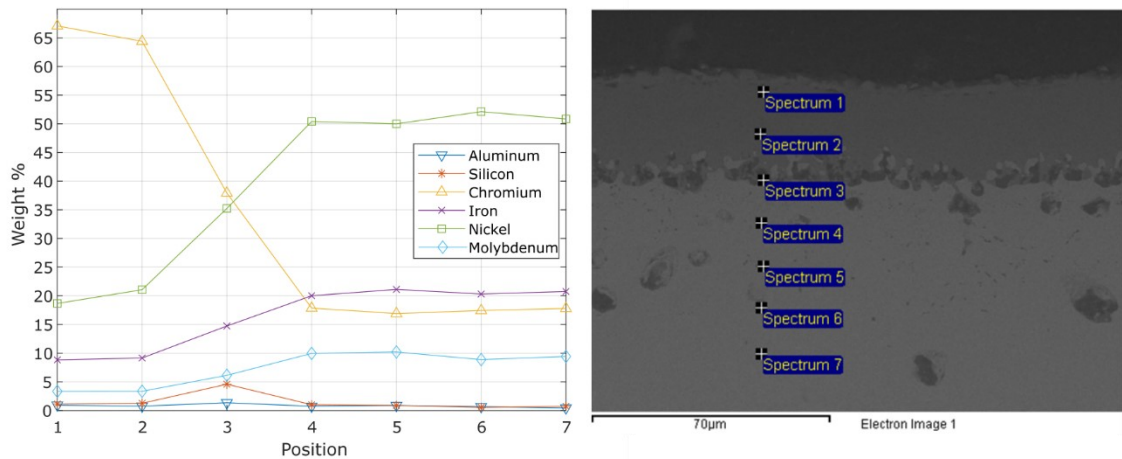


Figure 47: Quantitative EDS analysis across the oxide-substrate interface of a wrought sample after 500 hours (oxygen omitted).

The EDS analysis indicates a significant increase in chromium content in the oxide layer compared to the substrate in both the AM and the wrought samples. This suggests that the oxide layer is primarily composed of chromia, Cr_2O_3 . Literature suggests that the oxidation

of chromium typically occurs at oxide-gas interface [82]. Therefore, the oxidation rate is controlled by the diffusion of chromium ions through the chromia layers. The presence of the other alloying elements (Fe and Ni) shown to decrease significantly across the metal-oxide interface. This indicates that Cr is the primary oxide formed in the scale.

At the metal-oxide interfaces different types of oxides can be observed, as shown in Figure 48. Along the interface, a significant number of voids are formed which appear as black spots in the SEM images. The voids were confirmed as such using back-scattered electrons (BSE) as well as a low vacuum secondary Tescan detector (LVSTD). It is also noted that a significant number of smaller voids are formed in the substrate itself due either pullout during polishing or Kirkendall phenomenon [83]. In the sample shown in Figure 48 the voids can be seen to penetrate the substrate beyond 40-45 μm .

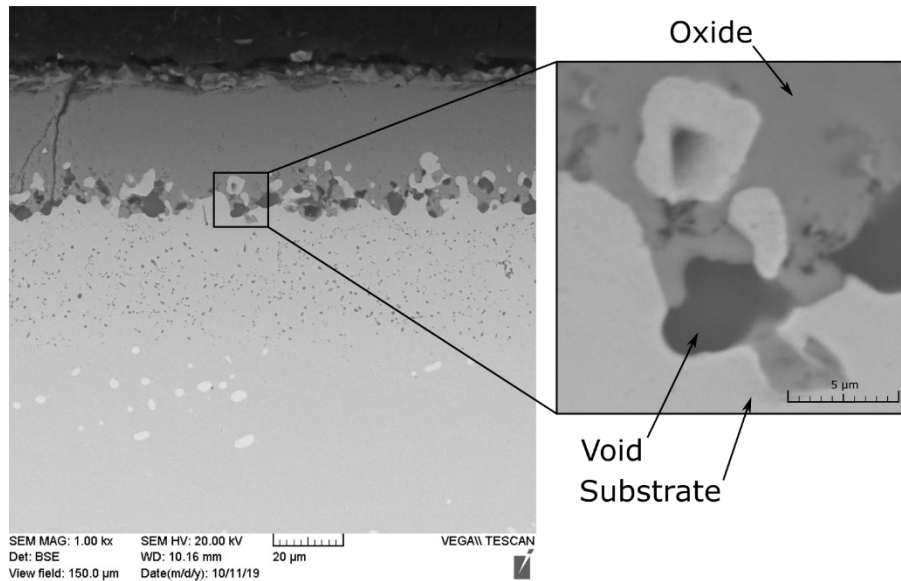


Figure 48: Detailed view of metal-oxide interface after 1000 hours of oxidation test.

The presence of cracks within the oxide layer is quite common among all samples, particularly in 500-hour and 1000-hour samples. The likelihood of spallation increases over time as the number of cracks increase. Figure 49 shows a wrought sample with a number of cracks perpendicular and parallel to the metal-oxide surface. Crack formations such as these can cause material ejection during the cooling to room temperature or material loss during the handling of the specimens. In addition, when cracks and spallation begin to occur, the protective nature of the oxide will be reduced, and the oxidation will likely increase.

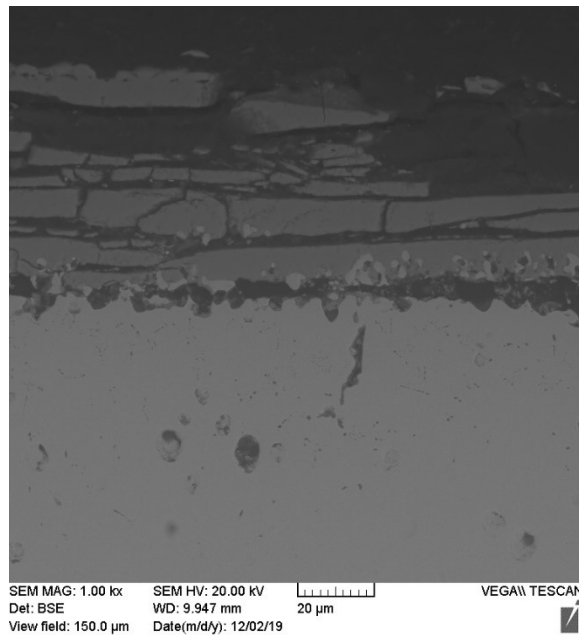


Figure 49: Location of spallation in wrought sample after 500 hours.

Chapter 5: Concluding Remarks and Future Work

In this research, the wire and arc additive manufacturing process for superalloy Hastelloy X was developed and characterized. The effects of varying parameters in the TIG based process were investigated for single layer samples using the Taguchi method and an analysis of variance (ANOVA). Deposition strategies for multi-layer samples were also evaluated. Finally, the isothermal oxidation behavior of AM Hastelloy X was characterized and compared to the wrought alloy through experimentation. The conclusions of the research are summarized in the following sections.

5.1 Effects of WAAM Process Parameters

Qualitative and quantitative effects of TIG based WAAM process parameters on the attributes of the printed specimens were studied utilizing the test matrix outlined in Section 3.3. Samples were observed to have ‘humping’ and ‘undercutting’ in the substrate as well as a concentration of interfacial defects at the center of the bead-substrate interface due to the fluid flow during weld pool solidification. The presence of molybdenum carbides were confirmed using EDS analysis.

One-way ANOVA was performed to determine trends between each factor and response.

Significant trends were observed, including:

- Bead height increases linearly with wire feed rate. Both melt through depth and roughness are independent of wire feed rate.
- Bead width decreases with travel speed. Melt through depth reduces significantly with travel speed.

- Travel speed and current inversely affect heat input and therefore show similar trends except in opposite direction. Increasing travel speed or decreasing current results in a decrease in melt through depth and an increase in roughness.
- Argon flow rate produces no significant effects on the bead height, bead width, wetting angle, melt through depth, or roughness, suggesting that the argon flow rate can be maintained at a constant level determined by the need to prevent oxidation in future work.

5.2 Multi-layered Samples

Preliminary trials were used to gain knowledge of the process behavior during multi-layer sample manufacturing. Printing path strategies were first tested using three layered specimens and no significant difference was found between printing layers along the same direction or in alternating directions. In preliminary trials, no interpass pause time was used which led to no observable interface between the layers, suggesting a complete fusion between layers with no noticeable oxidation.

Additionally, due to the excessive heat input of the preliminary trials, three distinct zones were identified. In the first zone, nearest to the bead-substrate interface, the carbides are finer and evenly distributed amongst the columnar grain matrix. The second zone includes larger and less evenly distributed carbides. Finally, in the third zone, the carbides return to a fine and evenly distributed manner within a cellular grain structure. The microstructure was improved in subsequent samples by reducing heat input to avoid excessive carbide growth however a post additive manufacturing heat treatment was also used to redistribute

the carbides and homogenize the microstructure. Future work can be conducted to investigate predicting or manipulating the microstructure of parts using process parameters and deposition strategies.

By refining deposition strategies and process parameters, the resulting multi-layer samples exhibited much less variation in the size and shape of the molybdenum carbides suggesting that the heat input was reduced sufficiently such that the previous layers were only remelted superficially during subsequent deposition. Hardness testing was conducted to confirm that there is little to no variation in hardness along or across the print direction, suggesting that the thermal history within the specimen was either relatively constant throughout or does not significantly impact the hardness of the specimen.

Suggested future work includes performing ANOVA using the Taguchi method to determine the effects of multi-layer process variables including interpass pause time, heat input reduction, and post-AM heat treatment on measured responses such as geometric tolerances, mechanical and fatigue properties, or residual stress and distortion. Additionally, future work would benefit from the addition of simple finite element analysis to model heat dissipation within the sample and substrate during deposition and predict residual stresses and distortion.

5.3 Isothermal Oxidation Testing

AM and wrought Hastelloy X samples were subjected to isothermal oxidation in air at 1080°C in order to compare oxidation resistance. The AM samples exhibited a parabolic

oxidation behavior with a rate constant, k_1 , of $4.54 \times 10^{-8} \text{ g}^2/\text{cm}^4/\text{h}$. Published values of the parabolic rate constant for wrought Hastelloy X are slightly higher than the experimental value obtained in this study, indicating that the AM samples may have an advantage in oxidation resistance due to finer grains and perhaps a better composition uniformity.

SEM imaging was used to measure oxide thicknesses which was observed to grow rapidly before reaching an asymptotic limit as the protective surface oxide forms and acts to impede the diffusion of chromium ions. EDS analysis confirmed that the oxide layer is primarily composed of chromia, Cr_2O_3 . In the substrate, near the metal-oxide interface, a significant number of smaller voids are formed due either carbide pullout during polishing or Kirkendall phenomenon and can be seen penetrating up to 40-45 μm from the interface.

References

- [1] S. Ford and M. Despeisse, “Additive Manufacturing and Sustainability: An Exploratory Study of the Advantages and Challenges,” *J. Clean. Prod.*, vol. 137, pp. 1573–1587, Nov. 2016.
- [2] W. Gao *et al.*, “The Status, Challenges, and Future of Additive Manufacturing in Engineering,” *Comput. Des.*, vol. 69, pp. 65–89, Dec. 2015.
- [3] T. D. Ngo, A. Kashani, G. Imbalzano, K. T. Q. Nguyen, and D. Hui, “Additive Manufacturing (3D printing): A Review of Materials, Methods, Applications and Challenges,” *Compos. Part B Eng.*, vol. 143, no. February, pp. 172–196, Jun. 2018.
- [4] W. E. Frazier, “Metal Additive Manufacturing: A Review,” *J. Mater. Eng. Perform.*, vol. 23, no. 6, pp. 1917–1928, Jun. 2014.
- [5] R. Reed, “Single-Crystal Superalloys for Blade Applications,” in *The Superalloys: Fundamentals and Applications*, Cambridge: Cambridge University Press, 2006, pp. 121–211.
- [6] ASTM International, “ASTM ISO/ASTM52900-15 Standard Terminology for Additive Manufacturing – General Principles – Terminology,” *ASTM International*. West Conshohocken, PA, 2015.
- [7] J. Gardan, “Additive Manufacturing Technologies,” in *Additive Manufacturing Handbook*, 1st Editio., A. Badiru, V. V. Valencia, and D. Liu, Eds. Boca Raton: CNC Press, 2017, pp. 150–168.
- [8] I. Gibson, D. Rosen, and B. Stucker, “Powder Bed Fusion Processes,” in *Additive Manufacturing Technologies: 3D Printing, Rapid Prototyping, and Direct Digital Manufacturing*, New York, NY: Springer New York, 2015, pp. 107–145.

- [9] L. C. Ardila *et al.*, “Effect of IN718 Recycled Powder Reuse on Properties of Parts Manufactured by Means of Selective Laser Melting,” *Phys. Procedia*, vol. 56, no. C, pp. 99–107, 2014.
- [10] K. L. Terrassa, J. C. Haley, B. E. MacDonald, and J. M. Schoenung, “Reuse of Powder Feedstock for Directed Energy Deposition,” *Powder Technol.*, vol. 338, pp. 819–829, Oct. 2018.
- [11] I. Gibson, D. W. Rosen, and B. Stucker, “Sheet Lamination Processes,” in *Additive Manufacturing Technologies: Rapid Prototyping to Direct Digital Manufacturing*, Boston, MA: Springer US, 2010, pp. 223–252.
- [12] G. H. Loh, E. Pei, D. Harrison, and M. D. Monzón, “An Overview of Functionally Graded Additive Manufacturing,” *Addit. Manuf.*, vol. 23, no. July, pp. 34–44, Oct. 2018.
- [13] K. Taminger and R. Hafley, “Electron Beam Freeform Fabrication: A Rapid Metal Deposition Process,” in *Proceedings of the 3rd Annual Automotive Composites Conference*, 2003.
- [14] S. W. Williams, F. Martina, A. C. Addison, J. Ding, G. Pardal, and P. Colegrove, “Wire + Arc Additive Manufacturing,” *Mater. Sci. Technol.*, vol. 32, no. 7, pp. 641–647, 2016.
- [15] B. Baufeld, E. Brandl, and O. van der Biest, “Wire Based Additive Layer Manufacturing: Comparison of Microstructure and Mechanical Properties of Ti–6Al–4V Components Fabricated by Laser-Beam Deposition and Shaped Metal Deposition,” *J. Mater. Process. Technol.*, vol. 211, no. 6, pp. 1146–1158, Jun. 2011.
- [16] C. Körner, “Additive Manufacturing of Metallic Components by Selective Electron

- Beam Melting — A Review,” *Int. Mater. Rev.*, vol. 61, no. 5, pp. 361–377, Jul. 2016.
- [17] H. Lee, C. H. J. Lim, M. J. Low, N. Tham, V. M. Murukeshan, and Y.-J. Kim, “Lasers in Additive Manufacturing: A Review,” *Int. J. Precis. Eng. Manuf. Technol.*, vol. 4, no. 3, pp. 307–322, Jul. 2017.
- [18] A. S. Haselhuhn, “Design for Low-Cost Gas Metal Arc Weld-Based Aluminum 3-D Printing,” Michigan Technological University, 2016.
- [19] A. A. Antonysamy, “Microstructure, Texture and Mechanical Property Evolution during Additive Manufacturing of Ti6Al4V Alloy for Aerospace Applications,” The University of Manchester, 2012.
- [20] J. N. Stavinoha, “Investigation of Plasma Arc Welding as a Method for the Additive Manufacturing of Ti-6Al-4V Alloy Components,” University of Montana, 2012.
- [21] J. L. Prado-Cerqueira, J. L. Diéguez, and A. M. Camacho, “Preliminary Development of a Wire and Arc Additive Manufacturing System (WAAM),” *Procedia Manuf.*, vol. 13, pp. 895–902, 2017.
- [22] W. Yangfan, C. Xizhang, and S. Chuanchu, “Microstructure and Mechanical Properties of Inconel 625 Fabricated by Wire-Arc Additive Manufacturing,” *Surf. Coatings Technol.*, vol. 374, no. October 2018, pp. 116–123, Sep. 2019.
- [23] ASTM, “Committee F42 on Additive Manufacturing Technologies,” 2019. .
- [24] T. Kellner, “The FAA Cleared the First 3D Printed Part to Fly in a Commercial Jet Engine from GE,” *GE Reports*, 2015. [Online]. Available: <https://www.ge.com/reports/post/116402870270/the-faa-cleared-the-first-3d-printed-part-to-fly-2/>.

- [25] T. Kellner, “World’s First Plant to Print Jet Engine Nozzles in Mass Production,” *GE Reports*, 2014. [Online]. Available: World’s First Plant to Print Jet Engine Nozzles in Mass Production.
- [26] Norsk Titanium, “Norsk Titanium Delivers First FAA-Certified, Additive Manufactured Ti64 Structural Aviation Components,” Jun-2017. [Online]. Available: <https://www.norsktitanium.com/media/press/norsk-titanium-delivers-first-faa-certified-additive-manufactured-ti64-structural-aviation-components>.
- [27] Sciaky Inc., “Sciaky’s Electron Beam Additive Manufacturing (EBAM) Process Achieves Qualification for Huge Satellite Fuel Tanks,” 2018. [Online]. Available: <https://www.sciaky.com/news/press-releases/223-sciaky-s-electron-beam-additive-manufacturing-ebam-process-achieves-qualification-for-huge-satellite-fuel-tanks>.
- [28] R. W. Messler, “Electric Arc Welding Processes,” in *Principles of Welding: Processes, Physics, Chemistry, and Metallurgy*, Weinheim, Germany: Wiley-VCH Verlag GmbH, 1999, pp. 40–93.
- [29] S. Ríos, P. A. Colegrove, F. Martina, and S. W. Williams, “Analytical Process Model for Wire + Arc Additive Manufacturing,” *Addit. Manuf.*, vol. 21, pp. 651–657, May 2018.
- [30] F. Martina, J. Mehnert, S. W. Williams, P. Colegrove, and F. Wang, “Investigation of the Benefits of Plasma Deposition for the Additive Layer Manufacture of Ti–6Al–4V,” *J. Mater. Process. Technol.*, vol. 212, no. 6, pp. 1377–1386, Jun. 2012.
- [31] F. Martina, “Investigation of Methods to Manipulate Geometry, Microstructure and Mechanical Properties in Titanium Large Scale Wire + Arc Additive Manufacturing,” Cranfield University, 2014.

- [32] L. Wang, J. Xue, and Q. Wang, "Correlation Between Arc Mode, Microstructure, and Mechanical Properties During Wire Arc Additive Manufacturing of 316L Stainless Steel," *Mater. Sci. Eng. A*, vol. 751, no. February, pp. 183–190, Mar. 2019.
- [33] S. Radel, A. Diourte, F. Soulié, O. Company, and C. Bordreuil, "Skeleton Arc Additive Manufacturing with Closed Loop Control," *Addit. Manuf.*, vol. 26, no. July 2018, pp. 106–116, Mar. 2019.
- [34] Y. Luo, J. Li, J. Xu, L. Zhu, J. Han, and C. Zhang, "Influence of Pulsed Arc on the Metal Droplet Deposited by Projected Transfer Mode in Wire-Arc Additive Manufacturing," *J. Mater. Process. Technol.*, vol. 259, no. April, pp. 353–360, Sep. 2018.
- [35] J. Lin *et al.*, "Microstructural Evolution and Mechanical Property of Ti-6Al-4V Wall Deposited by Continuous Plasma Arc Additive Manufacturing Without Post Heat Treatment," *J. Mech. Behav. Biomed. Mater.*, vol. 69, no. June 2016, pp. 19–29, May 2017.
- [36] J. J. Lin *et al.*, "Microstructural Evolution and Mechanical Properties of Ti-6Al-4V Wall Deposited by Pulsed Plasma Arc Additive Manufacturing," *Mater. Des.*, vol. 102, pp. 30–40, Jul. 2016.
- [37] E. A. Alberti, B. M. P. Bueno, and A. S. C. M. D'Oliveira, "Additive Manufacturing Using Plasma Transferred Arc," *Int. J. Adv. Manuf. Technol.*, vol. 83, no. 9–12, pp. 1861–1871, Apr. 2016.
- [38] Sciaky Inc., "Benefits of Wire vs. Powder Metal 3D Printing." [Online]. Available: <https://www.sciaky.com/additive-manufacturing/wire-vs-powder>. [Accessed: 12-Jan-2020].

- [39] J. Zhang, X. Wang, S. Paddea, and X. Zhang, "Fatigue Crack Propagation Behaviour in Wire+Arc Additive Manufactured Ti-6Al-4V: Effects of Microstructure and Residual Stress," *Mater. Des.*, vol. 90, pp. 551–561, Jan. 2016.
- [40] P. A. Colegrove *et al.*, "Microstructure and Residual Stress Improvement in Wire and Arc Additively Manufactured Parts Through High-Pressure Rolling," *J. Mater. Process. Technol.*, vol. 213, no. 10, pp. 1782–1791, Oct. 2013.
- [41] Q. Wu, T. Mukherjee, C. Liu, J. Lu, and T. DebRoy, "Residual Stresses and Distortion in the Patterned Printing of Titanium and Nickel Alloys," *Addit. Manuf.*, vol. 29, no. July, Oct. 2019.
- [42] T. A. Rodrigues, V. Duarte, J. A. Avila, T. G. Santos, R. M. Miranda, and J. P. Oliveira, "Wire and Arc Additive Manufacturing of HSLA Steel: Effect of Thermal Cycles on Microstructure and Mechanical Properties," *Addit. Manuf.*, vol. 27, no. February, pp. 440–450, May 2019.
- [43] B. Wu *et al.*, "A Review of the Wire Arc Additive Manufacturing of Metals: Properties, Defects and Quality Improvement," *J. Manuf. Process.*, vol. 35, no. February, pp. 127–139, Oct. 2018.
- [44] J. F. Rudy and E. J. Rupert, "Effects of Porosity on Mechanical Properties of Aluminum Welds," *Am. Weld. Soc.*, vol. July, pp. 322–336, 1970.
- [45] G. Mathers, "Welding Metallurgy," in *The Welding of Aluminium and its Alloys*, Elsevier, 2002, pp. 10–34.
- [46] R. W. Messler, "Molten Metal and Weld Pool Reactions," in *Principles of Welding: Processes, Physics, Chemistry, and Metallurgy*, Weinheim, Germany: Wiley-VCH Verlag GmbH, 1999, pp. 315–358.

- [47] C. Zhang, M. Gao, and X. Zeng, “Workpiece Vibration Augmented Wire Arc Additive Manufacturing of High Strength Aluminum Alloy,” *J. Mater. Process. Technol.*, vol. 271, no. October 2018, pp. 85–92, Sep. 2019.
- [48] J. Gu, S. Yang, M. Gao, J. Bai, Y. Zhai, and J. Ding, “Micropore Evolution in Additively Manufactured Aluminum Alloys Under Heat Treatment and Inter-Layer Rolling,” *Mater. Des.*, vol. 186, no. November, p. 108288, Jan. 2020.
- [49] N. Rodriguez, L. Vázquez, I. Huarte, E. Arruti, I. Tabernero, and P. Alvarez, “Wire and Arc Additive Manufacturing: A Comparison Between CMT and TopTIG Processes Applied to Stainless Steel,” *Weld. World*, vol. 62, no. 5, pp. 1083–1096, Sep. 2018.
- [50] R. W. Messler, “Weld Fusion Zone Solidification,” in *Principles of Welding: Processes, Physics, Chemistry, and Metallurgy*, Weinheim, Germany: Wiley-VCH Verlag GmbH, 1999, pp. 373–453.
- [51] Y. Kok *et al.*, “Anisotropy and Heterogeneity of Microstructure and Mechanical Properties in Metal Additive Manufacturing: A Critical Review,” *Mater. Des.*, vol. 139, pp. 565–586, Feb. 2018.
- [52] “ISO/ASTM 52921:2013 Standard Terminology for Additive Manufacturing - Coordinate Systems and Test Methodologies.” ISO/ASTM, 2013.
- [53] J. F. Box, “R. A. Fisher and the Design of Experiments, 1922-1926,” *Am. Stat.*, vol. 34, no. 1, p. 1, Feb. 1980.
- [54] C. M. Borrór, “Design of Experiments Using the Taguchi Approach: Sixteen Steps to Product and Process Improvement,” *J. Qual. Technol.*, vol. 34, no. 4, pp. 462–463, Oct. 2002.

- [55] S. and S. R. S. Kalpakjian, “Quality Assurance, Testing, and Inspection,” in *Manufacturing Engineering & Technology*, 6th Editio., Addison-Wesley, 2009, pp. 1020–1048.
- [56] J. L. Devore, “Quality Control Methods,” in *Probability and Statistics for Engineering and Sciences*, Boston, MA: Brooks/Cole, 2010, pp. 651–687.
- [57] W. Betteridge and S. W. K. Shaw, “Development of Superalloys,” *Mater. Sci. Technol.*, vol. 3, no. 9, pp. 682–694, 1987.
- [58] R. C. Reed, *The Superalloys: Fundamentals and Applications*. Cambridge: Cambridge University Press, 2006.
- [59] J. B. Wahl and K. Harris, “New Single Crystal Superalloys, CMSX®-8 and CMSX®-7,” in *Superalloys 2012: 12th International Symposium on Superalloys2*, 2012, pp. 179–188.
- [60] Rolls Royce Ltd., *The Jet Engine*. Derby, England: Rolls-Royce, 1996.
- [61] S. H. Chen, S. C. Su, P. C. Chang, S. Y. Chou, and K. K. Shieh, “The Machinability of MAR-M247 Superalloy,” *Adv. Eng. Forum*, vol. 1, pp. 155–159, Sep. 2011.
- [62] G. R. Thellaputta, P. S. Chandra, and C. S. P. Rao, “Machinability of Nickel Based Superalloys: A Review,” *Mater. Today Proc.*, vol. 4, no. 2, pp. 3712–3721, 2017.
- [63] S. S. Florjancic, J. Pross, and U. Eschbach, “Rotor Design in Industrial Gas Turbines,” in *International Gas Turbine & Aeroengine Congress & Exhibition*, 1997.
- [64] W. Endres, “Rotor Design for Large Industrial Gas Turbines,” in *International Gas Turbine and Aeroengine Congress and Exposition*, 1992.
- [65] J. M. Kalinowski, “Weldability of a Nickel-Based Superalloy,” 1994.

- [66] Haynes International, “HASTELLOY ® X Alloy,” 2017. [Online]. Available: http://www.haynesintl.com/alloys/alloy-portfolio_/High-temperature-Alloys/HASTELLOY-X-alloy/HASTELLOY-X-principal-features.aspx. [Accessed: 02-Jun-2018].
- [67] J.-C. Zhao, M. Larsen, and V. Ravikumar, “Phase Precipitation and Time–Temperature-Transformation Diagram of Hastelloy X,” *Mater. Sci. Eng. A*, vol. 293, no. 1–2, pp. 112–119, Nov. 2000.
- [68] C. Shen *et al.*, “The Influence of Post-Production Heat Treatment on the Multi-Directional Properties of Nickel-Aluminum Bronze Alloy Fabricated Using Wire-Arc Additive Manufacturing Process,” *Addit. Manuf.*, vol. 23, no. July, pp. 411–421, Oct. 2018.
- [69] N. Birks, G. H. Meier, and F. S. Pettit, “Mechanisms of Oxidation,” in *Introduction to the High-Temperature Oxidation of Metals*, Cambridge: Cambridge University Press, 2006, pp. 39–74.
- [70] N. Birks, G. H. Meier, and F. S. Pettit, “Oxidation of Pure Metals,” in *Introduction to the High-Temperature Oxidation of Metals2*, Cambridge: Cambridge University Press, 2006, pp. 75–100.
- [71] S. Samal, “High-Temperature Oxidation of Metals,” in *High-Temperature Corrosion and Materias Applications*, ASM International, 2016.
- [72] N. V. Kazantseva, N. N. Stepanova, and M. B. Rigmant, “Nickel Superalloys,” in *Superalloys: Analysis and Control of Failure Process*, CRC Press, 2019, pp. 1–130.
- [73] G. Y. Lai, “Oxidation,” in *High-Temperature Corrosion And Materials Applications*, ASM International, 2007, pp. 5–66.

- [74] M. Danielewski, "Kinetics of Gaseous Corrosion," in *Corrosion: Fundamentals, Testing and Protection*, 13A ed., ASM International, 2003.
- [75] C. L. Angerman, "Long-Term Oxidation of Superalloys," *Oxid. Met.*, vol. 5, no. 2, pp. 149–167, Nov. 1972.
- [76] ASM International, "Weld Solidification," in *Weld Integrity and Performance*, S. Lampman, Ed. Novelty, Ohio: ASM International, 1997, p. 19.
- [77] K. C. Mills, B. J. Keene, R. F. Brooks, and A. Shirali, "Marangoni Effects in Welding," *Philos. Trans. R. Soc. A Math. Phys. Eng. Sci.*, vol. 356, no. 1739, pp. 911–925, 1998.
- [78] C. R. Heiple and J. R. Roper, "Mechanism for Minor Element Effect on GTA Fusion Zone Geometry," *Weld. J.*, vol. 61, no. 4, pp. 97–102, 1982.
- [79] D. Tomus, Y. Tian, P. A. Rometsch, M. Heilmaier, and X. Wu, "Influence of Post Heat Treatments on Anisotropy of Mechanical Behaviour and Microstructure of Hastelloy-X Parts Produced by Selective Laser Melting," *Mater. Sci. Eng. A*, vol. 667, pp. 42–53, 2016.
- [80] D. M. England, "Oxidation Kinetics of Some Nickel-Based Superalloy Foils and Electronic Resistance of the Oxide Scale Formed in Air Part I," *J. Electrochem. Soc.*, vol. 146, no. 9, p. 3196, 1999.
- [81] N. Parimin, E. Hamzah, and A. Amrin, "Effect of Grain Size on the Isothermal Oxidation of Fe-33Ni-19Cr Alloys at 700 °C," *Adv. Mater. Res.*, vol. 845, pp. 56–60, Dec. 2013.
- [82] W. C. Hagel and A. U. Seybolt, "Cation Diffusion in Cr₂O₃," *J. Electrochem. Soc.*, vol. 108, no. 12, pp. 1146–1152, 1961.

- [83] B. Pieraggi, "Diffusion and Solid State Reactions," in *Developments in High Temperature Corrosion and Protection of Materials*, Elsevier, 2008, pp. 9–35.